Journal of Materials Chemistry B

ROYAL SOCIETY OF CHEMISTRY

PAPER

View Article Online
View Journal | View Issue

Cite this: J. Mater. Chem. B, 2023, 11, 3453

Combined chemo-immuno-photothermal therapy based on ursolic acid/astragaloside IV-loaded hyaluronic acid-modified polydopamine nanomedicine inhibiting the growth and metastasis of non-small cell lung cancer†

Fan Xu,‡[a] Minghua Li,‡[a] Zujun Que,[b] Mingliang Su,[c] Wang Yao,[c] Yu Zhang,[c] Bin Luo,[a] Yan Li,[a] Zhanxia Zhang *[c] and Jianhui Tian*[ab]

Combining chemotherapy and immunotherapy is a promising strategy for the treatment of non-small cell lung cancer (NSCLC) metastasis. However, platinum-based chemotherapeutics and immune checkpoint blockade-based cancer immunotherapy have toxic side effects and limitations. Ursolic acid (UA) and astragaloside IV (AS-IV) are natural compounds with anticancer activity sourced from Traditional Chinese medicine (TCM). However, their poor water solubilities and targeted deletions limit their medicinal value. In this study, we fabricated hyaluronic acid (HA)-modified UA/(AS-IV)-loaded polydopamine (PDA) nanomedicine (UA/(AS-IV)@PDA-HA) with a high yield at a low cost *via* simple synthesis. This represents a novel multifunctional nanomedicine that combines chemotherapy, photothermal therapy (PTT), and immunotherapy with an active tumor-targeting ability. The as-prepared nanomedicine not only increased the aqueous solubilities of UA and AS-IV, but also improved their active targeting abilities. HA binds specifically to the overexpressed cluster of differentiation 44 (CD44) on the surface of most cancer cells, thereby improving drug targeting. While evaluating the anticancer effect of UA/(AS-IV)@PDA-HA *in vitro* and *in vivo*, the PDA nanodelivery system significantly improved UA-mediated cytotoxicity and anti-metastatic ability against NSCLC cells. In addition, the system also improved the AS-IV-mediated self-immune response of tumor-related antigens, which further inhibited the growth and distant metastasis of NSCLC. Further, PDA nanomaterial-mediated PTT inhibited tumor growth substantially. UA/(AS-IV)@PDA-HA not only significantly eradicated the primary tumor but also strongly inhibited the distant metastasis of NSCLC *in vitro* and *in vivo*. Thus, it has immense potential for development as an efficient anti-metastatic agent for NSCLC.

Received 26th October 2022,
Accepted 31st December 2022

DOI: 10.1039/d2tb02328h

rsc.li/materials-b

1. Introduction

Lung cancer is characterized by malignant tumors that originate from the bronchial mucosa or glands. According to the latest large-scale epidemiological survey (185 countries across six continents), lung cancer remains the highest ranked in terms of cancer-related mortality.[1,2] Non-small cell lung cancer (NSCLC) is a major pathological type of lung cancer, accounting for approximately 85% of all lung cancer cases.[3] The disordered proliferation and metastasis of cancer cells cause high mortality, severely affecting the prognosis, survival, and quality of life of patients with NSCLC. Currently, effective clinical prevention and treatment measures for this disease are lacking. Platinum-based chemotherapy regimens have long been recognized as a first-line treatment of NSCLC, to ensure anti-proliferation and anti-metastasis of NSCLC. Immunotherapy has become a hot topic in the field of NSCLC treatment in recent years and can significantly improve the immunosuppressive tumor microenvironment by inhibiting the growth and metastasis of NSCLC cells.[4] Current immunotherapies, including chimeric antigen

[a] Clinical Oncology Center, Shanghai Municipal Hospital of Traditional Chinese Medicine, Shanghai University of Traditional Chinese Medicine, Shanghai 200071, China. E-mail: tjhhawk@shutcm.edu.cn
[b] Institute of Oncology, Shanghai Municipal Hospital of Traditional Chinese Medicine, Shanghai University of Traditional Chinese Medicine, 200071, Shanghai, China
[c] Institute of Traditional Chinese Medicine Oncology, Longhua Hospital, Shanghai University of Traditional Chinese Medicine, 200032, Shanghai, China. E-mail: zhanxiazhang@shutcm.edu.cn

† Electronic supplementary information (ESI) available. See DOI: https://doi.org/10.1039/d2tb02328h

‡ Fan Xu and Minghua Li contributed equally to this work.

receptor T-cell, checkpoint-blockade therapy, cytokine therapy, and cancer vaccines, have been established as promising cancer treatments. In this context, the combination of chemotherapy and immunotherapy has brought hope to patients with NSCLC.[5–7] The rationale behind this strategy lies in the use of drugs that work through different mechanisms, thereby decreasing the likelihood of NSCLC growth and metastasis and is a more effective strategy than administering each treatment alone. However, current platinum-based chemotherapy regimens for NSCLC have limitations, including toxic side effects, multi-drug resistance, and off-target effects in patients.[8,9] The clinical application of immunotherapies, such as programmed death-1 (PD-1) and programmed cell death-ligand 1 (PD-L1), is also limited by variations in the therapeutic responses of individual patients, as well as non-specific inflammation, autoimmunity, and extremely high costs. Anti-tumor efficacy is observed only in 20–30% of patients with NSCLC, with most patients not achieving objective responses.[10,11] These issues seriously limit the efficacy and clinical applicability of NSCLC.

Traditional Chinese medicine (TCM) is a rich resource for drug discovery. Natural compounds extracted from TCM have potential clinical applications with lower rates of toxicity and higher efficiencies and could be used to overcome existing bottlenecks in traditional anticancer therapeutics.[12–18] Ursolic acid (UA) is a member of the triterpenoid molecular family and exists in medicinal herbs in free form or as aglycones of triterpenoid saponins. Studies have shown that the pharmacological actions of UA include antibacterial, anticancer, anti-inflammatory,[19] sedative, and hypoglycemic effects.[20] At present, the anti-tumor effects of UA are receiving increasing attention,[21] with several studies confirming that UA inhibits proliferation, promotes apoptosis,[22] and mediates metastasis through its associated signaling pathway[23] as a chemotherapeutic agent. Astragaloside IV (AS-IV) is the major pharmacologically active ingredient extracted from astragalus and belongs to the chemical class of triterpenes. Previous studies have demonstrated that AS-IV is an excellent immunotherapeutic agent. Studies have shown that AS-IV can efficiently decrease the proportion of Tregs and increase cytotoxic T cells (CTLs) by interfering with the IDO signaling pathway.[24] In addition, AS-IV inhibits lung cancer progression and metastasis by modulating macrophage polarization through the AMPK signaling pathway.[25] Thus, AS-IV exhibits significant anti-tumor and anti-metastatic effects by overcoming the immunosuppressive mechanisms mediated by tumors, eliciting robust and durable anticancer immunity, inhibiting tumor progression, and prolonging survival. Thus, AS-IV shows great promise in anticancer immunotherapy. The combination of the chemotherapeutic agent UA and the immune therapeutic agent AS-IV kills NSCLC cells directly and activates various signaling pathways and the systemic immune response, further inhibiting the growth and avoiding distant metastasis of NSCLC. These mechanisms directly compensate for the shortcomings of traditional anticancer therapeutics, namely toxic side effects and individual variations in therapeutic responses.

However, the poor aqueous solubilities and non-specific biodistribution patterns of free UA and AS-IV contribute to their low bioavailability *in vivo*, restricting their clinical application. Therefore, an adaptive drug delivery system is required to address this issue. In recent years, increasing efforts have been devoted to the development of nano-drug delivery systems. Nanotechnology has distinct advantages over conventional drug delivery methods, including a high drug loading efficiency, tumor-targeting capability, the co-delivery of multiple drugs, a long circulation time, decreased drug resistance, and diminished systemic adverse effects,[26] which could facilitate the clinical efficacy of anticancer drugs by further improving drug delivery efficiency.[27,28] Since 1995, anti-tumor nano-drugs including Mvocet, Doxil, Mvocet, and DepoCyt are available in the market. Research in the field of nano-drug delivery systems has favorable prospects for clinical applications. Therefore, we focused on the preparation of a novel nano-delivery system to improve the therapeutic efficacy of UA and AS-IV in inhibiting lung cancer proliferation and metastasis.[29] Polydopamine (PDA) is an oxidative polymeric product of dopamine hydrochloride (DA). DA has strong molecular adsorption capacity for most inorganic and organic materials. DA self-polymerizes to form surface-adherent PDA films on a wide range of materials (*i.e.*, organic and inorganic) *via* a spontaneous oxidation reaction in an alkaline solution; this makes it stable enough to reach the target cells.[30–32] PDA has good water solubility, which remarkably enhances the aqueous solubility of otherwise insoluble drugs. PDA also contains numerous functional groups, such as catechol and amine groups. As a result, PDA can be easily surface-modified. In addition, PDA is extremely sensitive to pH, self-assembling at alkaline pH and rapidly disintegrating at acidic pH. Thus, PDA is prone to releasing loaded drugs in acidic tumor microenvironments or lysosomes. Furthermore, PDA exhibits low toxicity and excellent biodegradability. PDA also has strong passive tumor-targeting properties owing to the enhanced permeability and retention (EPR) effect. Studies have shown that PDA nano-drug delivery systems have a high drug-loading efficiency, representing a promising nano-drug delivery system. More importantly, PDA is a highly efficient photothermal agent due to its excellent optical-to-thermal energy conversion efficiency. The complex aggregation mode during the formation of PDA enables photothermal conversion, allowing for photothermal therapy (PTT) under 808 nm laser irradiation.[33] PTT effectively converts a near-infrared (NIR) laser into thermal energy and directly kills local tumor cells, representing a novel non-invasive therapeutic technology. It is typically administered after surgical treatment, radiotherapy, chemotherapy, or biological treatment and overcomes the toxic side effects of anticancer drugs. Hence, PTT is considered to be one of the most efficient cancer treatments.[34,35] PTT agents include carbon-based nanoparticles, noble metal nanomaterials, black phosphorus, and some semiconductors.[36–39] As an NIR-absorbing nanomaterial, PDA shows high photothermal conversion efficiency in the NIR region, which can be used to precisely destroy cancer cells using locally raised temperatures. Hyaluronic acid (HA) is a component of the extracellular matrix (ECM) and a high-molecular-weight glycoprotein with hydrophilic properties and can enclose hydrophobic molecules to enhance hydrophilicity. It is extensively used as a vehicle for the specific targeting of the CD44 receptor,

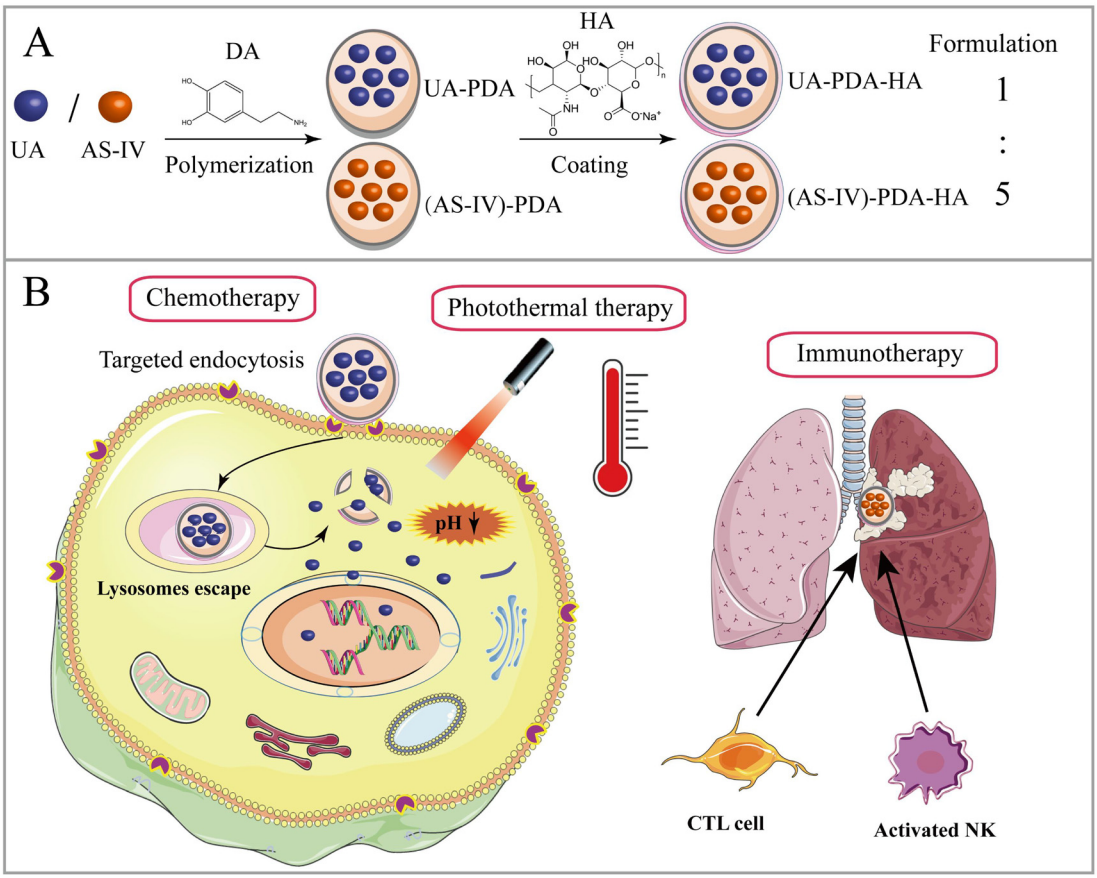

Scheme 1 (A) Schematic illustration of the key steps toward the synthesis of core–shell UA/(AS-IV)@PDA-HA nanomedicine. (B) Schematic illustration of UA/(AS-IV)@PDA-HA nanomedicine combined chemo-immuno-photothermal therapy in inhibiting the growth and metastasis of lung cancer.

which is overexpressed in NSCLC cells.[40,41] HA-modified nanomaterials can achieve active tumor targetability.[42–44]

In this paper, we report a new tumor-targeted nanomedicine that combines chemotherapy, immunotherapy, and PTT, wherein DA self-polymerizes under alkaline conditions and forms a DA nanocoating on the surfaces of UA and AS-IV (UA/(AS-IV)@PDA). The synthesized nanomedicine was found to improve the water solubility and passive targeting ability of UA and AS-IV. Thereafter, HA was added to the surface of the UA/(AS-IV)@PDA, further enhancing the active tumor-targeting property of the nanoparticles (Scheme 1(A)). The inhibition of NSCLC growth and metastasis was evaluated *in vitro* and *in vivo* through a series of experiments. Our preliminary results show that fabricated hyaluronic acid (HA)-modified UA/(AS-IV)-loaded polydopamine (PDA) nanomedicine (UA/(AS-IV)@PDA-HA) not only effectively inhibited the growth of primary tumors, but also strongly inhibited the distant metastasis of NSCLC. UA/(AS-IV)@PDA-HA showed excellent inhibitory effects on the growth and metastasis of lung cancer *in vivo* and *in vitro* compared with free UA/(AS-IV). The active targeting and PTT properties of the nanomedicine were evaluated *in vitro* and *in vivo*. PDA nanomaterial-mediated PTT and HA-mediated active targeting resulted in a highly efficient synergistic anticancer effect (Scheme 1(B)).

2. Materials and methods

2.1 Materials

UA, AS-IV, DA, sodium salt of HA (40–100 kDa, 97%), and dimethyl sulfoxide (DMSO) were purchased from Macklin (Shanghai, China). Hochest-33258 and tris-buffered saline (TBS) were purchased from Solarbio (Beijing, China). Cell Counting Kit-8 (CCK-8) was obtained from Biosharp (Beijing, China). Ammonium hydroxide ($NH_3 \cdot H_2O$), sodium hydroxide (NaOH), and Rhodamine B (Rh B) were obtained from Aladdin (Shanghai, China). Ethyl alcohol (EOH) was purchased from Titian (Shanghai, China). Lyso-tracker Green, Annexin-V-FITC apoptosis detection kit, and calcein-AM/PI staining kit were purchased from Beyotime Biotech (Shanghai, China). Antibody against β-actin was obtained from HuaBio (Hangzhou, China). Antibody against CD44 was obtained from GeneTex (USA). Matrigel-356234, FITC anti-mouse CD3, PE anti-mouse CD8a, APC anti-mouse CD4, and PE-CF594 Mouse Anti-Mouse NK1.1 were purchased from BD (USA), while alanine transaminase (ALT), aspartate aminotransferase (AST), and creatinine (CRE) activity assay kits were obtained from JianCheng Bioengineering Institute (Nanjing, China). High-glucose Dulbecco's modified Eagle's medium (DMEM-High Glucose) was provided by Basal-Media (China), whereas Ham's F-12K (1×) medium was provided by Bioagrio (Shanghai, China). Fetal bovine serum (FBS)

and penicillin–streptomycin solution were purchased from Gibco (USA). Phosphate-buffered saline (PBS) was purchased from ServiceBio (Wuhan, China).

2.2 Cell lines and cell culture

The human lung circulating tumor cell line CTC-TJH-01 used in this study was obtained from the Jianhui Tian Research Group. It is the first human lung adenocarcinoma circulating tumor cell line in the world and was collected from the peripheral blood of female patients with stage IIA lung adenocarcinoma (Fig. S1, ESI†). Cells were cultured in Ham's F-12K (1×) medium with 10% FBS and 1% penicillin–streptomycin solution. The normal human bronchial epithelial cell line BEAS-2B, the human lung adenocarcinoma cell line A549 and the murine lung cancer cell line LLC-luc were purchased from the American Type Culture Collection (Manassas, VA, United States). Cells were maintained in high-glucose DMEM containing 10% FBS and 1% penicillin–streptomycin solution. Cells were grown in a carbon dioxide (CO_2) incubator (Heracell 240 i; Thermo Scientific, Germany) at 37 °C with 5% CO_2.

2.3 Cytotoxicity assay of UA and AS-IV

The *in vitro* cytotoxicities of UA and AS-IV were evaluated using CCK-8 assays. LLC-luc and CTC-TJH-01 in log growth phase were seeded into 96-well plates at a density of 3×10^3 cells per well and incubated in a CO_2 incubator at 37 °C with 5% CO_2 for 12 h. Then, UA or AS-IV was added to wells in medium supplemented with 10% FBS at different concentrations and incubated for 48 h. Next, the original medium was removed, and 90 μl fresh medium and 10 μl of CCK-8 solution were added to each well. The cells were further cultured for another 1 h in a CO_2 incubator at 37 °C with 5% CO_2. Finally, the optical density (OD) of each well was measured at 450 nm using a multiwell plate reader (Synergy HTX; BioTek, USA). Untreated cells in growth media were used as blank controls.

2.4 Evaluation of the synergistic effects of UA and AS-IV

A single concentration of UA was combined with different concentrations of AS-IV to evaluate the synergistic effects of UA and AS-IV. The cell viability in each experimental group was evaluated using the CCK-8 assay. Three data points were used for each drug for each experiment. The non-constant-ratio combination was chosen to determine the effects of both drugs in combination. The synergistic effect between UA and AS-IV was presented by the half maximal inhibitory concentration (IC_{50}) and the coefficient of drug interaction (CDI) value. CDI was determined using eqn (1):

$$\mathrm{CDI} = \frac{AB}{A \times B} \quad (1)$$

where *AB* is the ratio of the viability of cells treated with the UA/(AS-IV) combination to that of the control groups and *A* or *B* is the ratio of the viability of cells treated with only UA or AS-IV to that of the control group, respectively. CDI > 1 indicates antagonism and CDI < 1 indicates synergism; CDI = 1 indicates additivity and CDI < 0.7 indicates significant synergism.

2.5 Preparation of UA/(AS-IV)@PDA-HA

An alkaline alcohol aqueous solution was prepared using 10 ml of distilled water (dH_2O), 5 ml of EOH, and 200 μl of $NH_3 \cdot H_2O$. The solution was magnetically stirred at room temperature (25 °C ± 5 °C) for 5 min. Subsequently, 50 mg of UA was added to the solution. The system was stirred for 2 h to ensure good dispersion. Thereafter, 100 mg of DA was dissolved in dH_2O and slowly added to the solution. The color of the solution quickly transformed from colorless to dark, indicating oxidative self-polymerization of DA and the continuous formation of UA-loaded PDA nanoparticles (UA@PDA). The reaction mixture was then stirred for 12 h at room temperature (25 °C ± 5 °C). After the reaction, the UA@PDA was washed and centrifuged using a refrigerated high-speed centrifuge (AVANTI J-E; Beckman Coulter, USA) to remove any free nanostructures or UA. To modify the targeting molecule HA, 15 mg of HA was added to 15 ml of TBS (pH = 8.5) with strong shaking to dissolve it completely before adding it to the obtained UA@PDA under stirring for another 4 h. Finally, UA-loaded HA-modified PDA nanoparticles (UA@PDA-HA) were collected using a refrigerated high-speed centrifuge. This method was also used to synthesize (AS-IV)-loaded PDA nanoparticles (AS-IV)@PDA and (AS-IV)-loaded HA-modified PDA nanoparticles (AS-IV)@PDA-HA.

UA@PDA-HA and (AS-IV)@PDA-HA were broken by adding NaOH solution with a pH of more than 12 and centrifuging at 10 000 rpm for 20 min. The UA and AS-IV content in the nanomedicine was then measured by Liquid Chromatograph Mass Spectrometer (LC-MS) (API 4000; AB SCIEX, USA). The encapsulation efficiency (EE%) was calculated using eqn (2) and (3):

$$\mathrm{EE\%\ (UA)} = \frac{\text{UA encapsulated in nanomedicine}}{\text{Amount of UA added}} \times 100\% \quad (2)$$

$$\mathrm{EE\%\ (AS\text{-}IV)} = \frac{\text{AS-IV encapsulated in nanomedicine}}{\text{Amount of AS-IV added}} \times 100\% \quad (3)$$

Finally, UA/(AS-IV)@PDA-HA was formulated by mixing the two nanoparticles in a 1 : 5 UA/AS-IV molar ratio.

2.6 Characterization of UA/(AS-IV)@PDA-HA

2.6.1 Transmission electron microscopy (TEM). UA@PDA-HA and (AS-IV)@PDA-HA were visualized using negative staining electron microscopy. Five microliters of the diluted samples was separately deposited onto copper TEM grids for 1 min. After sample absorption, the surplus was removed using a filter paper, followed by the addition of 5 μl of 2% uranyl acetate for 1 min. After surplus removal, the samples were dried at room temperature (25 °C ± 5 °C) and examined by TEM (JEM-1230; JEOL, Japan).

2.6.2 Scanning electron microscopy (SEM). Drops of the prepared samples were spotted onto carbon-coated copper grids and allowed to dry at room temperature (25 °C ± 5 °C).

A high-resolution scanning electron microscope (Sigma300; Zeiss, Germany) was used to investigate the morphology of UA@PDA-HA and (AS-IV)@PDA-HA.

2.6.3 Determination of particle size and zeta potential. The nanoparticle size was observed using SEM and analyzed using a particle size analyzer (Nano Measurer 1.2). The zeta potential was measured by the wet method using a Zetasizer (Mastersizer 2000; Malvern, UK). The instrument was performed following the manufacturer's instructions in triplicate, and values are expressed as mean ± standard deviation (SD).

2.6.4 Fourier-transform infrared spectroscopy (FTIR). Infrared spectra (FTIR) were obtained using a Fourier transform infrared spectrometer (Nicolet iS 5; Thermo Scientific, USA). Then, 1 ml of prepared suspension was dripped onto a glass slide, forming a thick film after allowing to air dry for 5 min. The composite films were then placed directly on the ATR crystal and analyzed. Spectra were collected over a range of 4000–500 cm^{-1}. Three samples were examined under the same conditions for each material and the final average spectrum was calculated.

2.7 *In vitro* release of UA in UA@PDA-HA and release of AS-IV in (AS-IV)@PDA-HA

The UA@PDA-HA and (AS-IV)@PDA-HA were sealed in dialysis bags (molecular weight cutoff: 1000 Da), after which the bags were placed in different centrifuge tubes. A total of 8 ml of PBS with different pH levels (7.2 and 5.5) was added to each tube. All centrifuge tubes were shaken, and 1 ml of the supernatant buffer was collected at predetermined time intervals. Release of the UA and AS-IV were detected with a LC-MS (API 4000; AB SCIEX, USA).

2.8 *In vitro* photothermal property and photothermal stability measurement

First, the photothermal properties of UA/(AS-IV)@PDA-HA were evaluated. Five groups (1 ml per group) were included, as follows: (i) PBS group; (ii) free UA/(AS-IV) group; (iii) blank PDA-HA group; (iv) UA/(AS-IV)@PDA group; (v) UA/(AS-IV)@PDA-HA group (concentration 0.6 mg ml^{-1} UA and 5.6 mg ml^{-1} AS-IV). The solutions were then irradiated with an 808 nm laser at 1.0 W cm^{-2} predetermined photodensity for 10 min. The laser-irradiation-induced temperature elevation was recorded every minute using an infrared (IR) camera (Fotric 220; Fotric, USA). To evaluate the concentration-dependent photothermal property, 1 ml of aqueous dispersion of UA/(AS-IV)@PDA-HA at different concentrations was irradiated by an 808 nm laser (1.0 W cm^{-2}, 10 min). The following groups were evaluated: (i) PBS group; (ii) UA/(AS-IV)@PDA-HA group (0.15 mg ml^{-1} UA and 1.4 mg ml^{-1} AS-IV); (iii) UA/(AS-IV)@PDA-HA group (0.3 mg ml^{-1} UA and 2.8 mg ml^{-1} AS-IV); (iv) UA/(AS-IV)@PDA-HA group (0.6 mg ml^{-1} UA and 5.6 mg ml^{-1} AS-IV); (v) UA/(AS-IV)@PDA-HA group (1.2 mg ml^{-1} UA and 11.2 mg ml^{-1} AS-IV). The laser irradiation-induced temperature elevation was recorded every minute.

Next we measured the photothermal conversion efficiency of UA/(AS-IV)@PDA-HA. The prepared nanomedicine solution was placed in a 1 cm path length quartz cuvette. The temperature change in response to irradiation with an 808 nm laser (1.0 W cm^{-2}) was measured using the IR camera (Fotric 220; Fotric, USA). Photothermal conversion efficiency was calculated using the following:

$$\eta = \frac{hA(T_{max} - T_{surr}) - Q_s}{I(1 - 10^{-A_{808}})} \quad (4)$$

$$hA = \frac{m \times c_p}{\tau_s} \quad (5)$$

$$t = -\tau_s \ln \theta \quad (6)$$

$$\theta = \frac{\Delta T}{\Delta T_{max}} = \frac{T - T_{surr}}{T_{max} - T_{surr}} \quad (7)$$

The values of η were obtained from eqn (4)–(7). In equation, h is the heat transfer coefficient, A is the surface area of the container, m is the weight of the solvent and c_p is the specific heat capacity of water. τ_s is the time constant measured from the slope of linear regression line plotted by time t and $-\ln(\theta)$. T_{max} is the maximum steady-state temperature, and T_{surr} is the surround temperature. Q_s is the heat associated with the light absorbance of control sample (water) and quartz cuvette. I is the input power, and A_{808} is the absorbance of sample at 808 nm.

For photothermal stability, 1 ml of aqueous dispersion of UA/(AS-IV)@PDA-HA (0.6 mg ml^{-1} UA and 5.6 mg ml^{-1} AS-IV) was irradiated by the 808 nm laser (1.0 W cm^{-2}) for 10 min (laser on) and then natural cooled without irradiation for 10 min (laser off). Five on/off laser cycles were performed. During the experiment, the temperature of the aqueous dispersion was recorded to determine the photothermal stability of UA/(AS-IV)@PDA-HA.

2.9 *In vitro* biocompatibility

The *in vitro* biocompatibility of blank PDA-HA and 808 nm laser irradiation was evaluated using the CCK-8 assay. Cytotoxicity experiments were conducted using CTC-TJH-01, LLC-luc, and BEAS-2B cells. Cells in the exponential growth phase (3×10^3 cells per well) were seeded into 96-well plates in triplicate, and after incubation for 12 h to allow cell attachment, the cells were co-cultured with blank PDA-HA NPs at a series of indicated concentration gradients for another 48 h or treated with 808 nm laser irradiation (1.0 W cm^{-2}, 5 min). Then, 10 μl of the CCK-8 reagent was added to each well and incubated for 1 h. Absorbance was measured using a fluorescence microplate reader at 450 nm.

2.10 *In vitro* HA-mediated active targeting

2.10.1 Western blotting (WB). BEAS-2B, A549, CTC-TJH-01 and LLC-luc cells were inoculated in 60 mm^2 dishes at a density of 1×10^6 cells per dish. When the cells formed a confluent monolayer, the cells were treated with RIPA lysis buffer and the concentrations of extracted proteins were detected by a protein assay kit. The obtained samples were then subjected to WB to

detect CD44. The immunoreactive bands were filmed using a chemiluminescence image analysis system (Tanon, Shanghai, China) and finally semi-quantitated by ImageJ software 1.8.0.

2.10.2 Cellular uptake experiments. Cellular uptake experiments were performed to verify the targeting capacity of the HA. First, fluorescently labelled UA/(AS-IV)@PDA and UA/(AS-IV)@PDA-HA were prepared by adding Rh B for 12 h. The nanoparticles were then washed with PBS more than five times until no noticeable color change was observed in the supernatant fluids, followed by resuspension in F-12K or DMEM. BEAS-2B, A549 and CTC-TJH-01 cells were seeded into confocal dishes at 1×10^5 cells per well and LLC-luc cells were seeded into confocal dishes at 1.5×10^5 cells per well. After 12 h, the cells were co-cultured with either fluorescently labelled UA/(AS-IV)@PDA NPs for 4 h or fluorescently labelled UA/(AS-IV)@PDA-HA NPs for 2 h and 4 h. After incubation, the F-12K or DMEM was removed. The cells were washed three times with cold PBS. The cells were further stained with Lyso-Tracker® Green for 1 h, washed three times with cold PBS (pH 7.4), and stained with Hoechst for 15 min. Subsequently, these cells were fixed with 4% paraformaldehyde for 15 min. HA-mediated cellular targeting was then observed using confocal laser scanning microscopy (CLSM) (SP8; Leica, Germany) with a Cy3 channel for the nanoparticles, Oregon Green 488 channel for the lysosomes, and DAPI channel for the nucleus.

2.11 *In vitro* cell cytotoxicity assay

Cell cytotoxicity was measured using the CCK-8 assay and Calcein-AM/Propidium Iodide (Calcein-AM/PI) staining. For the CCK-8 assay, CTC-TJ-01 and LLC-luc cells were seeded into 96-well plates at 3×10^3 cells per well in triplicate and incubated for 12 h. After exposure to (i) fresh medium, (ii) free UA/(AS-IV), (iii) UA/(AS-IV)@PDA, (iv) UA/(AS-IV)@PDA-HA, and (v) UA/(AS-IV)@PDA-HA with 808 nm laser irradiation (1.0 W cm^{-2}, 5 min) for 48 h in the dark, cells were added 100 μl of fresh medium containing 10% CCK-8 solution. After incubation at 37 °C for another 1 h, the absorbance of the solution at 450 nm was measured using a multiwell-plate reader (Synergy HTX; BioTek, USA). Eqn (3) was used to calculate the cell viability (%):

$$\text{Cell viability}\,(\%) = \frac{(A_{\text{treat}} - A_0)}{(A_{\text{control}} - A_0)} \times 100\% \qquad (8)$$

where A_0, A_{treat}, and A_{control} represent the absorbance of the blank medium, treated cells, and untreated cells, respectively.

Calcein-AM/PI staining was performed to study the cytotoxicity of UA/(AS-IV)@PDA-HA. Briefly, CTC-TJH-01 and LLC-luc cells (3×10^5 cells per well) were seeded into 6-well plates and cultured for another 12 h. The cells were then treated with: (i) fresh medium, (ii) free UA/(AS-IV), (iii) UA/(AS-IV)@PDA, (iv) UA/(AS-IV)@PDA-HA, and (v) UA/(AS-IV)@PDA-HA with 808 nm laser irradiation (1.0 W cm^{-2}, 5 min) for 24 h. The cells were then stained with Calcein-AM/PI according to the manufacturer's instructions. Fluorescence images were obtained using a fluorescence microscope (DMI3000 B; Leica, Germany).

2.12 *In vitro* apoptosis assay

CTC-TJH-01 and LLC-luc cells (3×10^5 cells per well) were seeded into 6-well plates and incubated in 3 ml of medium. Twelve hours later, the medium was replaced and cells were treated with different formulations: (i) fresh medium, (ii) free UA/(AS-IV), (iii) UA/(AS-IV)@PDA, (iv) UA/(AS-IV)@PDA-HA, and (v) UA/(AS-IV)@PDA-HA with 808 nm laser irradiation (1.0 W cm^{-2}, 5 min) for 48 h. Thereafter, the cells were harvested, resuspended in Annexin V-FITC binding buffer, and stained with 5 μl of Annexin V-FITC and 10 μl of PI for 15 min in a dark environment according to the apoptosis Detection Kit. Finally, 1×10^4 cells were analyzed using a flow cytometer (DXFLEX; Beckman Coulter, USA).

2.13 *In vitro* cell migration assay

2.13.1 Wound healing assay. CTC-TJH-01 and LLC-luc were seeded into 6-well plates (1×10^6 cells per well) in complete medium and incubated at 37 °C in 5% CO_2. Once the cells formed a confluent monolayer, the medium was removed and the monolayers were scraped using a 200 μl pipette tip to create a "scratch". After rinsing the wells with cold PBS twice, the wells were treated with different reagents: (i) fresh medium, (ii) free UA/(AS-IV), (iii) UA/(AS-IV)@PDA, (iv) UA/(AS-IV)@PDA-HA, and (v) UA/(AS-IV)@PDA-HA with 808 nm laser irradiation (1.0 W cm^{-2}, 5 min), which were formulated with DMEM or F-12K (2% FBS medium and 1% penicillin–streptomycin solution). The cells were observed after 0 and 24 h of treatment. Images of the wound area were obtained using an optical microscope (Thermo EVOS XL Core Scientific). The degree of wound healing was evaluated as a percentage of wound healing, as follows (4):

$$A = \frac{(A_0 - A_1)}{A_0} \times 100\% \qquad (9)$$

The proportions of the initial scratch (A_0) and final scratch (A_1) were calculated using ImageJ software 1.8.0.

2.13.2 Transwell migration assay. The migration abilities of CTC-TJH-01 and LLC-luc cells were determined using 24-well Transwell chambers, with upper and lower culture compartments separated by polycarbonate membranes with 8 μm pores. Briefly, 1×10^5 CTC-TJH-01 cells were cultured in 100 μl of serum-free medium. The cells were then seeded into the upper chamber (8.0 μm pore) and co-cultured with different reagents: (i) fresh medium, (ii) free UA/(AS-IV), (iii) UA/(AS-IV)@PDA, (iv) UA/(AS-IV)@PDA-HA, and (v) UA/(AS-IV)@PDA-HA with 808 nm laser irradiation (1.0 W cm^{-2}, 5 min). The concentration of drugs used in migration assays is 2.129 μM (CTC-TJH-01, IC_{50} value of UA/(AS-IV)@PDA-HA + Laser group) and 2.147 μM (LLC-luc, IC_{50} value of UA/(AS-IV)@PDA-HA + Laser group). A total of 600 μl media (20% FBS) was placed in the lower well. After 24 h, cells on the upper surface of the membrane were carefully removed with a cotton swab, and migrant cells on the lower surface were fixed with 4% fresh paraformaldehyde at 37 °C for 15 min, followed by staining with 0.05% crystal violet for 30 min. Images were obtained

using an optical microscope. Three random microscopic fields (10×) of each membrane were chosen, and the metastatic cells were counted with ImageJ.

2.14 *In vitro* cell invasion assay

Cell invasion was evaluated using a Transwell invasion assay. Serum-free medium was added to dilute the Matrigel (1 : 4). Next, 25 μl of diluted Matrigel (1 mg ml^{-1}) was inoculated into each chamber and hardened in a CO_2 incubator for 2 h at 37 °C. Then, 100 μl of serum-free medium was added for 30 min at 37 °C. The remaining steps were the same as those used in the Transwell migration assay. The migrated cells were counted in three random fields (20× magnification) under an optical microscope. The average number of cells per field was calculated and quantified using ImageJ software.

2.15 Animals and tumor model

To establish xenograft tumor and lung metastasis models, six-week-old C57BL/6 male mice (~20 g) were purchased from Lingchang Biotechnology Co., Ltd (Shanghai, China) and maintained under standard housing conditions. Subcutaneous LLC-luc tumors were generated by subcutaneously injecting 3×10^5 LLC-luc (suspended in PBS) into the left side of the armpit. When the tumor volume reached 50 mm^3, the mice were randomly divided into different groups. All animal procedures were carried out according to the guidelines approved by the Animal Ethics Committee of the Shanghai University of Traditional Chinese Medicine.

2.16 *In vivo* PTT

The LLC-luc tumor-bearing mice were randomly divided into four groups and injected intraperitoneally with (i) saline (0.9% NaCl solution), (ii) free UA/(AS-IV), (iii) UA/(AS-IV)@PDA, or (iv) UA/(AS-IV)@PDA-HA (concentration: UA dose of 5 mg per kg bodyweight and a AS-IV dose of 25 mg per kg bodyweight). At 24 h post-intraperitoneal injection, each mouse was irradiated with an 808 nm laser (1.0 W cm^{-2}) for 5 min. The temperature of the tumor sites and infrared thermographic maps during PTT were monitored using an infrared thermal imaging camera (Fotric 220; Fotric, USA).

2.17 *In vivo* biodistribution of UA/(AS-IV)@PDA-HA

For biodistribution analysis, LLC-luc tumor-bearing mice were injected intraperitoneally with fluorescently labelled UA/(AS-IV)@PDA-HA. Fluorescent labelled UA/(AS-IV)@PDA-HA NPs were prepared by adding Rh B to the UA/(AS-IV)@PDA-HA solutions for 12 h, removing the excess dye molecules by centrifugation, and washing with water more than five times until no noticeable color change was observed in the supernatant fluids. At the pre-planned time points (0, 24, and 36 h), the main organs (heart, liver, spleen, lung, and kidney) and tumors were harvested. Subsequently, the fluorescence intensity in these organs and tumors was analyzed at 0, 24, and 36 h using a VISQUE *in vivo* imaging system (VISQUE® Invivo Smart-LF VIE-WORKS, Inc., USA) in the PE (red) channel.

In addition, HA-mediated active targeting *in vivo* was also validated. LLC-luc tumor-bearing mice were separated into two groups. After the tumor volume reached approximately 200–300 mm^3, the mice were injected intraperitoneally with (i) fluorescently labelled UA/(AS-IV)@PDA or (ii) fluorescently labelled UA/(AS-IV)@PDA-HA. Fluorescent labelled UA/(AS-IV)@PDA NPs and UA/(AS-IV)@PDA-HA NPs were prepared in the same way as above. After 24 h, the main organs (heart, liver, spleen, lung, and kidney) and tumors were harvested. Subsequently, the fluorescence intensity in these organs and tumors was quantitatively analyzed using the VISQUE *in vivo* imaging system (VISQUE® Invivo Smart-LF VIE-WORKS, Inc., USA) in the PE (red) channel to assess the HA-mediated active targeting *in vivo*.

2.18 *In vivo* anti-tumor and anti-metastasis ability

The *in vivo* therapeutic effect of UA/(AS-IV)@PDA-HA was evaluated in LLC-luc tumor-bearing mice. Briefly, the mice were stochastically divided into five groups (n = 6): (i) saline (0.9% NaCl solution) group, (ii) free UA/AS-IV group, (iii) UA/(AS-IV)@PDA group, (iv) UA/(AS-IV)@PDA-HA group, and (v) UA/(AS-IV)@PDA-HA group with 808 nm laser irradiation (1 W cm^{-2}, 5 min). Treatments were diluted in 0.9% NaCl solution and administered at a UA dose of 5 mg per kg bodyweight and an AS-IV dose of 25 mg per kg bodyweight. The mice were intraperitoneally injected every two days during a 21 day experimental period. Tumor volume and body weight were measured every two days. Tumor volumes were measured using Vernier calipers and evaluated using the following formula: (major diameter) × (minor diameter)^2/2. After 21 d, orbital blood was obtained from all mice before sacrifice, which was mainly used for the detection of hepatorenal function. The main organs and tumors were harvested and used for histological analysis by H&E staining of the thin transverse sections.

2.19 Immunohistochemical staining

The tumors and main organs in each group were fixed overnight with 4% paraformaldehyde. Then, the samples were dehydrated in ethanol, embedded in paraffin, and sectioned at a thickness of 5 μm. Next, the sections were deparaffinized in xylene and ethanol and rehydrated in water. Subsequently, antigen retrieval was performed by heating the samples in a microwave for 30 min in sodium citrate buffer (pH 6.0). Slides were then quenched in hydrogen peroxide (3%) to block endogenous peroxidase activity and washed with TBST buffer. Finally, the primary antibodies were incubated at 4 °C overnight, followed by analysis using a Polymer Detection kit (Life Technologies), according to the manufacturer's instructions, along with antibodies against cleaved caspase-3 (Abcam), Ki-67, CD8, and NK1.1.

2.20 Statistical analysis

All experiments were independently repeated in triplicate. All data are presented as mean ± SD. Statistically significant differences between two groups were analyzed using t-test, while statistically significant differences between multiple

groups were compared using one-way analysis of variance (ANOVA). Statistical analyses were performed using GraphPad Prism 7.0 (GraphPad Software, USA). $p < 0.05$ was considered statistically significant in all analyses (95% confidence level). $^{*}p < 0.05$, $^{**}p < 0.01$, $^{***}p < 0.001$, and $^{****}p < 0.0001$.

3. Results and discussion

3.1 Synergistic anti-tumor effect between UA and AS-IV

To detect the cytotoxicity of UA, CTC-TJH-01 and LLC-luc cells were incubated with different concentrations of UA. UA showed an obvious inhibitory effect on CTC-TJH-01 (Fig. 1(A)) and LLC-luc (Fig. 1(B)). Low concentrations of UA were found to inhibit cell activity in the concentration range of 1–5 μM, and cell proliferation gradually slowed down as the concentration increased. Above 40 μM, UA showed significant cytotoxicity to cells. The IC_{50} values (48 h) were 29.18 μM on CTC-TJH-01 and 43.87 μM on LLC-luc, respectively. The result showed that UA significantly inhibited the proliferation of NSCLC cells.

The inhibitory effect of AS-IV on NSCLC cell proliferation was also explored. Compared to the solvent control, different doses of AS-IV (8, 16, 31, 63, 125, and 250 μM) did not significantly inhibit the activity of CTC-TJH-01 (Fig. 1(C)) or LLC-luc (Fig. 1(D)). Furthermore, AS-IV did not induce any remarkable decrease in cell viability in CTC-TJH-01 or LLC-luc cells, demonstrating that it does not exert any direct cytotoxicity on lung cancer cells within a concentration interval of 0–250 μM.

Previous experiments have shown that UA monotherapy could inhibit the proliferation of CTC-TJH-01 and LLC-luc cells, while AS-IV alone did not significantly reduce cell survival after 48 h of treatment. Studies have also reported that both UA and AS-IV can enhance the sensitivity of cancer cells to chemotherapeutic drugs, such as cisplatin. To identify the synergistic anti-tumor activity between UA and AS-IV, we combined a single concentration of UA with varying concentrations of AS-IV for 48 h and performed the CCK-8 assay to evaluate the cytotoxicity of CTC-TJH-01 and LLC-luc. Subsequently, the IC_{50} and CDI values were calculated to determine whether the cytotoxic effects were synergistic. A CDI value <1 demonstrated a synergistic cytotoxic effect. The results showed that the combination of UA and AS-IV (1 : 1, 1 : 2, and 1 : 5 molar ratio) led to lower IC_{50} and CDI values in CTC-TJH-01 and LLC-luc cells compared to UA monotherapy (Fig. 1(E) and (F)). This indicates synergistic anti-tumor activity between UA and AS-IV, resulting in improved anti-tumor efficacy. Furthermore, combination at a molar ratio of 1 : 5 (UA : AS-IV = 1 : 5) was found to have an optimal synergistic effect (IC_{50} value [48 h] of 25.322 μM for CTC-TJH-01 and 25.799 μM for LLC-luc; the CDI value of 0.868 for CTC-TJH-01 and 0.610 for LLC-luc).

3.2 Synthesis and characterization of UA@PDA-HA and (AS-IV)@PDA-HA

In this study, UA/(AS-IV)@PDA-HA was constructed using a simple three-step synthetic procedure (Scheme 1(A)). First, UA or AS-IV was encapsulated in DA in an aqueous alkaline alcohol solution. Subsequently, the surfaces of the nanoparticles were modified with HA. According to LC-MS detection, the encapsulation efficiency of UA@PDA-HA was calculated to be 24% and (AS-IV)@PDA-HA was 58% (Fig. S2, ESI†). Finally, UA/(AS-IV)@PDA-HA was formulated by mixing the two nanoparticles at a molar ratio of 1 : 5 (UA : AS-IV).

The nanomedicines were characterized after their synthesis. The TEM and SEM images revealed that the obtained UA@PDA-HA and (AS-IV)@PDA-HA had a spherical morphology, a relatively homogeneous distribution of grain size, and good dispersibility in water (Fig. 2(A)). The particle sizes of UA@PDA-HA and (AS-IV)@PDA-HA were analyzed using SEM (Fig. 2(D)), and the resulting size distribution curves showed that the mean particle sizes of UA@PDA-HA and (AS-IV)@PDA-HA were

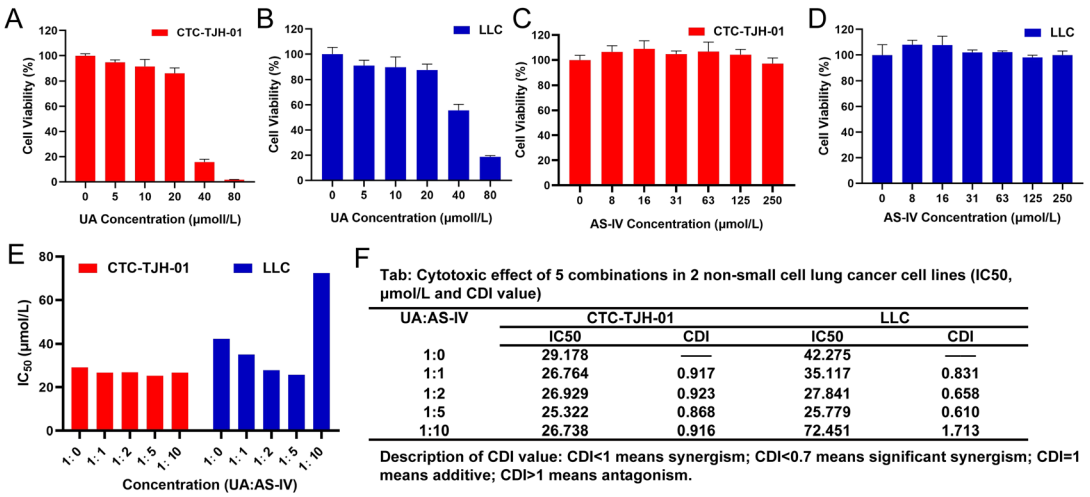

F

Tab: Cytotoxic effect of 5 combinations in 2 non-small cell lung cancer cell lines (IC50, μmol/L and CDI value)

UA:AS-IV	CTC-TJH-01		LLC	
	IC50	CDI	IC50	CDI
1:0	29.178	——	42.275	——
1:1	26.764	0.917	35.117	0.831
1:2	26.929	0.923	27.841	0.658
1:5	25.322	0.868	25.779	0.610
1:10	26.738	0.916	72.451	1.713

Description of CDI value: CDI<1 means synergism; CDI<0.7 means significant synergism; CDI=1 means additive; CDI>1 means antagonism.

Fig. 1 Synergistic effect evaluation of UA and AS-IV. (A) CCK-8 cell survival rate of CTC-TJH-01 after co-incubation with UA after 48 h. (B) CCK-8 cell survival rate of LLC-luc co-incubation with UA after 48 h. (C) CCK-8 cell survival rate of CTC-TJH-01 co-incubation with AS-IV after 48 h. (D) CCK-8 cell survival rate of LLC-luc co-incubation with AS-IV after 48 h. (E) and (F) Determination of the optimal proportions of UA and AS-IV for inducing the optimal synergistic effect (the IC_{50} value and the CDI value).

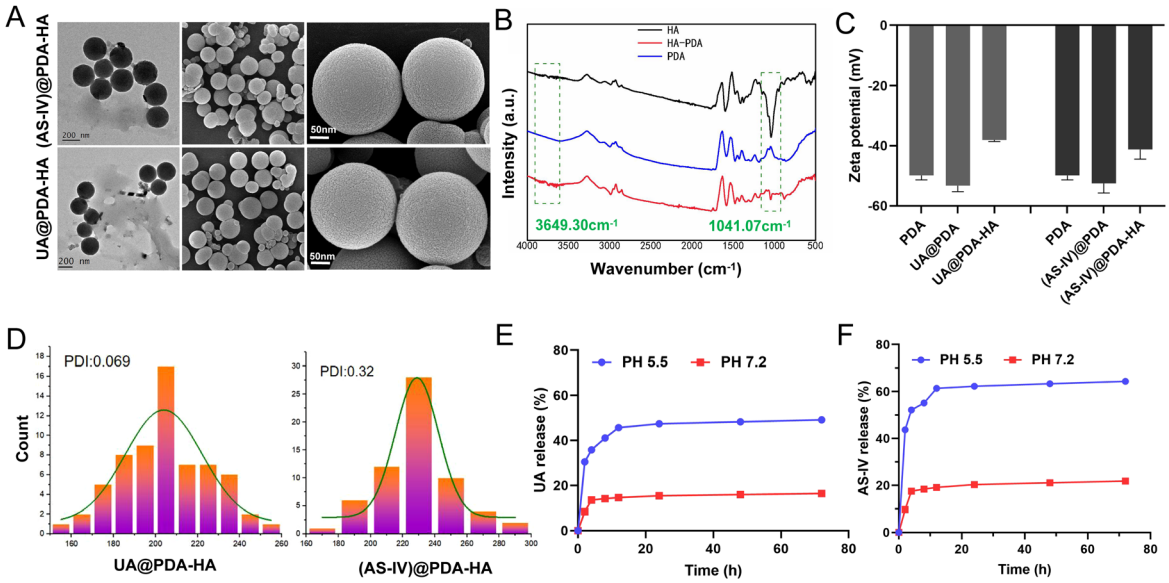

Fig. 2 Characterization of UA@PDA-HA and (AS-IV)@PDA-HA core–shell nanomedicine. (A) Representative transmission electron microscopy (TEM) and scanning electron microscopy (SEM) micrographs of UA@PDA-HA and (AS-IV)@PDA-HA showing the nanostructure, respectively. (B) Fourier transform infrared spectroscopy (FTIR) of PDA, HA and PDA-HA. (C) Zeta potential of PDA, UA@PDA, UA@PDA-HA, (AS-IV)@PDA and (AS-IV)@PDA-HA. (D) The size distribution curves and polydisperse indexes (PDI) of UA@PDA-HA and (AS-IV)@PDA-HA. (E) UA and (F) AS-IV release curves at different pH levels (5.5 and 7.2).

230 nm (PDI = 0.069) and 210 nm (PDI = 0.32), respectively. It has been shown that nanomedicines around 20–200 nm in size have good advantages in terms of overcoming cellular barriers and being internalised by cells. Therefore nanomedicines around 200 nm have better clinical translatability.

The zeta potentials of these nanoparticles in a neutral aqueous solution were also measured (Fig. 2(C)). The zeta potential of the PDA NPs, UA@PDA, and UA@PDA-HA were −49.9 mV, −53.3 mV, and −38.1 mV, respectively. The zeta potentials of the PDA NPs, (AS-IV)@PDA, (AS-IV)@PDA-HA were −49.9 mV, −52.5 mV, and −41.2 mV, respectively. All nanoparticles (PDA, UA@PDA, UA@PDA-HA, (AS-IV)@PDA, and (AS-IV)@PDA-HA) exhibited negative zeta potentials. The loading of UA or AS-IV during PDA synthesis led to a more negative zeta potential. In addition, the continuous surface coating of HA further lowered its zeta potential. The zeta potential changes indicated that UA and AS-IV were successfully embedded in the PDA nanoparticles, and the targeted molecule HA was effectively modified on the surface of UA@PDA and (AS-IV)@PDA.

To further verify the successful modification of the target drug molecule HA, an FTIR experiment was performed (Fig. 2(B)). The infrared spectrum of HA-loaded PDA exhibited characteristic peaks of 1041 cm^{-1} (HA, the asymmetric stretching peak of a carboxyl group) and 3649 cm^{-1} (HA, the hydrogen-bonded stretching vibration of –N–H or O–H), suggesting that HA was successfully loaded on the surface of the nanoparticles.

In vitro release of UA from UA@PDA-HA and AS-IV from (AS-IV)@PDA-HA in pH 7.2 and 5.5 were all investigated. The results exhibited that more UA and AS-IV were released in pH 5.5 than they were in pH 7.2. About 49.14% of UA and 64.4% of AS-IV were released in pH 5.5, whereas only 16.43% and 21.83% released in pH 7.2 (Fig. 2(E) and (F)). The results shows that UA/(AS-IV)@PDA-HA could achieve sustained release in the acidic environment of tumors.

3.3 *In vitro* photothermal effect and photothermal stability

To evaluate the *in vitro* photothermal conversion performance of the nanomedicine under 808 nm laser exposure, four groups were evaluated: (i) PBS buffer group, (ii) free UA/(AS-IV) group, (iii) UA/(AS-IV)@PDA group, and (iv) UA/(AS-IV)@PDA-HA group with 808 nm laser irradiation. The temperature of the different solutions under 808 nm laser exposure was monitored using IR thermal images (Fig. 3(A)). The temperature of the blank PDA-HA, UA/(AS-IV)@PDA, and UA/(AS-IV)@PDA-HA suspensions (0.3 mg ml^{-1} UA and 2.8 mg ml^{-1} AS-IV) was found to increase rapidly with time, gradually reaching a plateau at 52 °C, 54 °C, and 55 °C, respectively, under 808 nm (1.0 W cm^{-2}) laser irradiation for 10 min. However, negligible temperature increments were detected for PBS and free UA/(AS-IV) under 808 nm laser irradiation (1.0 W cm^{-2}, 10 min) (Fig. 2(B)). In addition, the temperature change curves of UA/(AS-IV)@PDA-HA (Fig. 3(C)) at various concentrations were measured with 808 nm laser irradiation, suggesting an obvious dose-dependent increase in the PTT effect. These findings demonstrate that PDA-induced PTT can efficiently and rapidly convert photo energy into heat under 808 nm laser irradiation. This may be because the electrons in PDA are excited by light energy, and the subsequent non-radiative relaxation generates heat. Therefore, the nanomedicine showed potential for PTT.

To evaluate photothermal stability, the temperature elevation profiles of blank PDA, UA/(AS-IV)@PDA and UA/(AS-IV)@PDA-HA

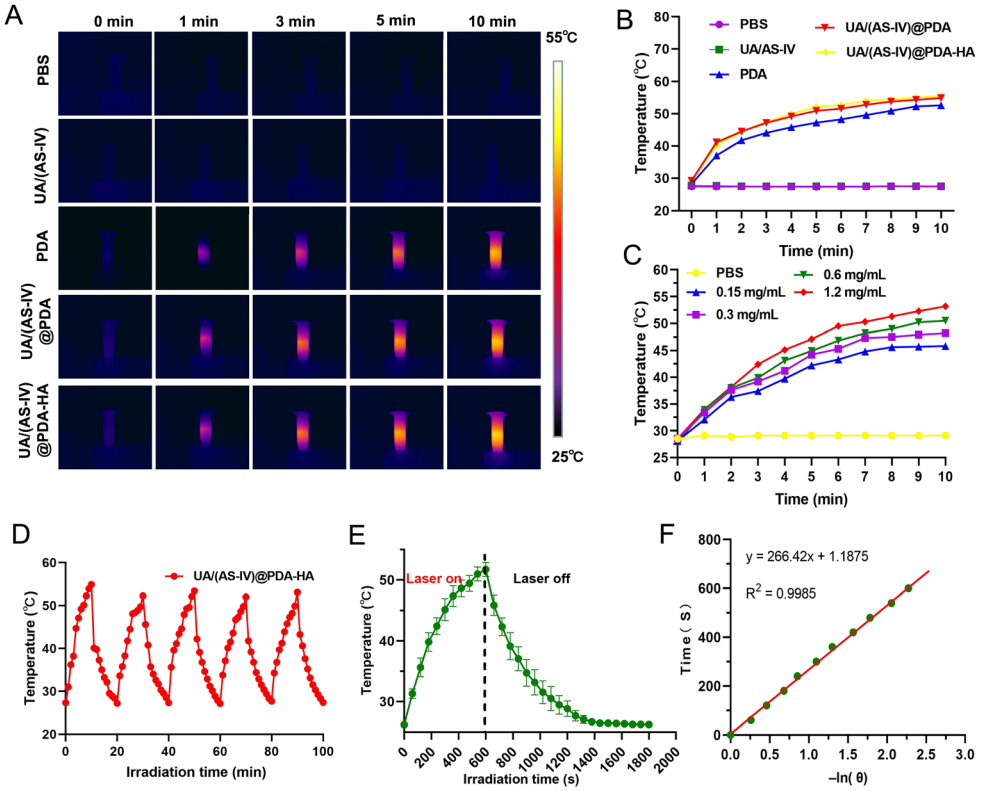

Fig. 3 *In vitro* photothermal effect and stability of UA/(AS-IV)@PDA-HA nanomedicine. (A) Infrared (IR) thermal images of PBS, free UA/(AS-IV), PDA, UA/(AS-IV)@PDA and UA/(AS-IV)@PDA-HA under the 808 nm laser irradiation (1 W cm^{-2}, 10 min). (B) The corresponding time-dependent temperature change curve. (C) Temperature elevation of UA/(AS-IV)@PDA-HA at different concentrations (0, 0.15, 0.3, 0.6, and 1.2 mg ml^{-1}) under the 808 nm laser (1 W cm^{-2}, 10 min). (D) Photothermal stability of UA/(AS-IV)@PDA-HA (0.6 mg ml^{-1}) for five consecutive photothermal cycles under 808 nm laser irradiation (1 W cm^{-2}). (E) and (F) Photothermal conversion efficiency of UA/(AS-IV)@PDA-HA. ***$p < 0.001$, ****$p < 0.0001$.

aqueous solution under five cycles of heating and cooling were recorded (Fig. S3, S4, ESI† and Fig. 3(D)). The temperature of the solution rapidly increased under 808 nm laser irradiation, whereas the temperature rapidly decreased after the irradiation was removed. No significant change was observed in the heating and cooling processes after five cycles, indicating that the nanomedicine had excellent photothermal stability. The photothermal properties and photothermal stability demonstrated that UA/(AS-IV)@PDA-HA can be adopted as a durable photoabsorbing agent for photonic cancer hyperthermia in the NIR-I biowindow.

The temperature of UA/(AS-IV)@PDA-HA reached 51.77 °C within 10 min in response to laser irradiation (Fig. 3(E)). The system time constant (τ) was calculated using the linear fitting graph of the cooling time and temperature change data (Fig. 3(F)). Based on these two results, we calculated the photothermal conversion efficiency of UA/(AS-IV)@PDA-HA. We calculated the photothermal conversion efficiency of UA/(AS-IV)@PDA-HA to be 42.83%.

3.4 *In vitro* biocompatibility

DA, a natural melanin, has been shown to have good biocompatibility as a nano-carrier. In theory, the metabolic products of DA are biodegradable homovanillic and trihydroxyphenylacetic acids. The potential toxicity of blank PDA-HA was determined using a cell viability assay against lung cancer CTC-TJH-01 and LLC-luc cell lines, as well as the normal lung BEAS-2B cell line. The CCK-8 results showed that the cell viability of BEAS-2B, CTC-TJH-01, and LLC-luc was higher than 80%, indicating the good biocompatibility of the PDA-HA nano-carrier (Fig. S5, ESI†). The results showed that the blank PDA had negligible cytotoxicity to both CTC-TJH-01 and LLC-luc at polymer concentrations of up to 200 μg mL^{-1}. Owing to its excellent photothermal conversion efficiency, blank PDA-HA was used as PTT agent. Then, the influence of the 808 nm laser on cell growth was also explored, which showed little potential toxicity to Bease2B, CTC-TJH-01, and LLC-luc without a photo-thermal reagent. Taken together, these results indicate that the blank nano-carrier and 808 nm laser irradiation have excellent biocompatibility.

3.5 HA-mediated targeted delivery of UA and AS-IV

Cellular uptake by tumor cells is an important factor that affects therapeutic efficacy. Enhancing cellular uptake efficiency is key to enhancing anti-tumor abilities. A large number of studies have shown that HA actively targets tumours by binding to CD44 receptors that are overexpressed on the surface of tumour cells. To verify HA-mediated active targeting, we first selected non-small cell lung cancer cell lines with different CD44 expression levels. The expression of CD44 in the four cell lines (BEAS-2B, CTC-TJH-01, A549, LLC-luc cell lines) were

verified by western blotting (Fig. 4(C) and (D)). The results showed that A549, CTC-TJH-01 and LLC-luc expressed CD44 at high level whereas BEAS-2B lacked CD44 expression. Furthermore, the expression level of CD44 were: A549 < CTC-TJH-01 < LLC-luc.

Then, a series of cellular uptake experiments were carried out to verify the active targeting effect of HA. BEAS-2B, A549, CTC-TJH-01 and LLC-luc were incubated with UA/(AS-IV)@PDA and UA/(AS-IV)@PDA, which were stained with Rh B with red fluorescence. As shown in the fluorescent images (Fig. 4(A) and (B)), stronger fluorescence of nanoparticles was observed in the cytoplasm and surrounding nuclear region in NSCLC cells (A549, CTC-TJH-01 and LLC-luc) in UA/(AS-IV)@PDA-HA 2 h group and UA/(AS-IV)@PDA-HA 4 h group, whereas lower fluorescence of nanoparticles was observed in UA/(AS-IV)@PDA 4 h group. In addition, the red fluorescence of Rh B from UA/(AS-IV)@PDA-HA after 2 h or 4 h was not significantly stronger than that from UA/(AS-IV)@PDA after 4 h in BEAS-2B cells. The fact that insignificant change observed in the BEAS-2B was attributed to non-specific endocytosis. In comparison, the UA/(AS-IV)@PDA-HA group showed a high level of endocytosis in NSCLC cells (A549, CTC-TJH-01 and LLC-luc), suggesting a specific tumor-targeting property of HA. These results indicate that the modification of HA markedly facilitated the endocytosis of tumor cells, strongly improving the tumor-targeted drug delivery ability of UA/(AS-IV)@PDA-HA.

3.6 *In vitro* anti-tumor effect

The *in vitro* anticancer effects were evaluated using the CCK-8 assay kit. Compared with the control group and the free UA/(AS-IV) group, the viability of the UA/(AS-IV)@PDA group was significantly reduced in CTC-TJH-01 (Fig. 5(A) and (B)) and LLC-luc (Fig. 5(C) and (D)) cells, demonstrating that the nano-drug delivery system improves the delivery of UA/(AS-IV)

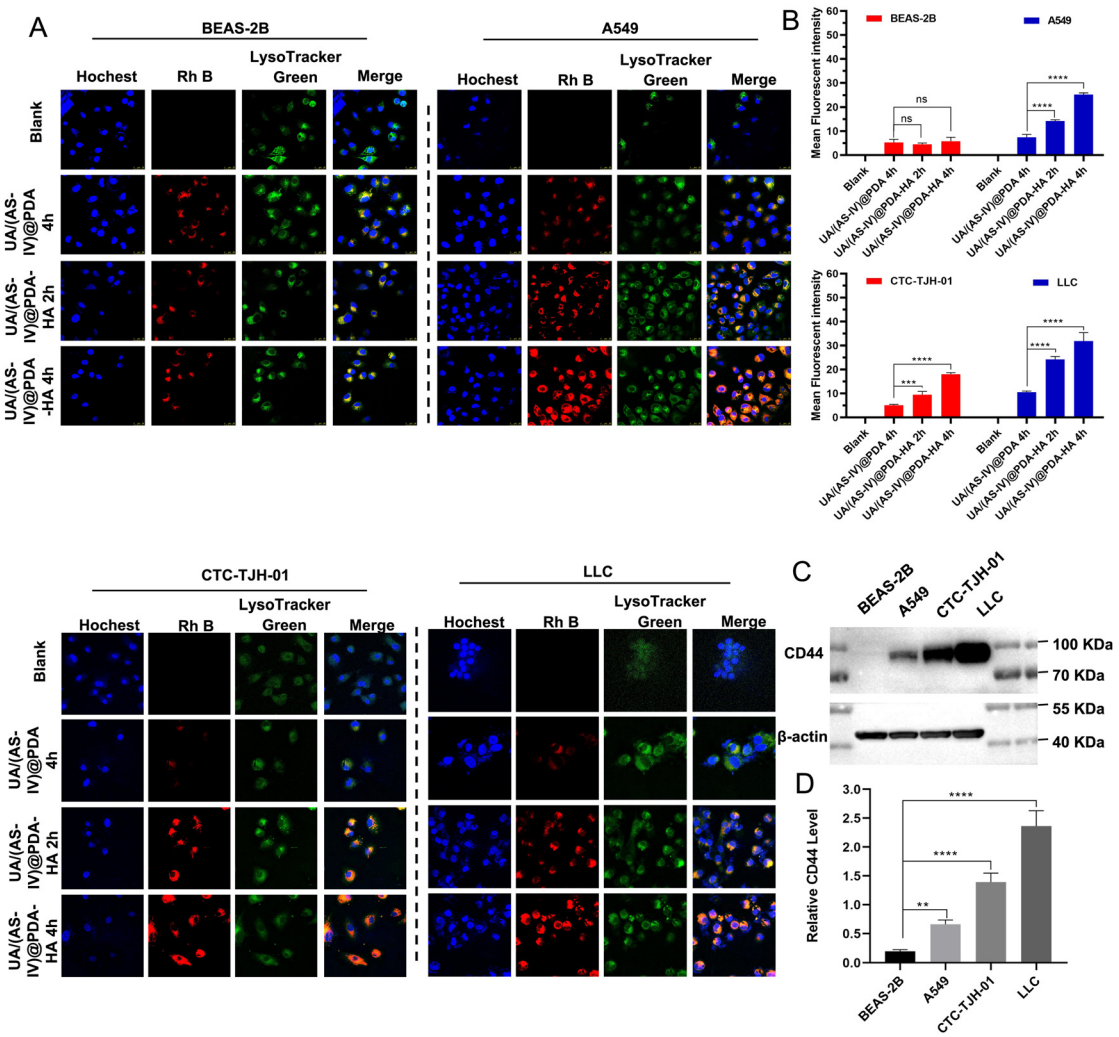

Fig. 4 *In vitro* targeting effect of HA-mediated nanomedicine. (A) CLSM images of BEAS-2B, A549, CTC-TJH-01, and LLC-luc incubated with unmodified PDA nanomedicine for 4 h and HA-modified PDA nanomedicine for 2 h or 4 h. The blue panel is Hoechst staining to represent the cell nucleus. The red panel is Rh B staining to represent the nanoparticles. The green panel is Lyso Tracker Green staining to represent the Lysosomes. (B) The corresponding fluorescence intensity after different treatments. (C) Western blot analysis and (D) the corresponding fluorescence intensity after different treatments.**$p < 0.01$, ***$p < 0.001$, ****$p < 0.0001$.

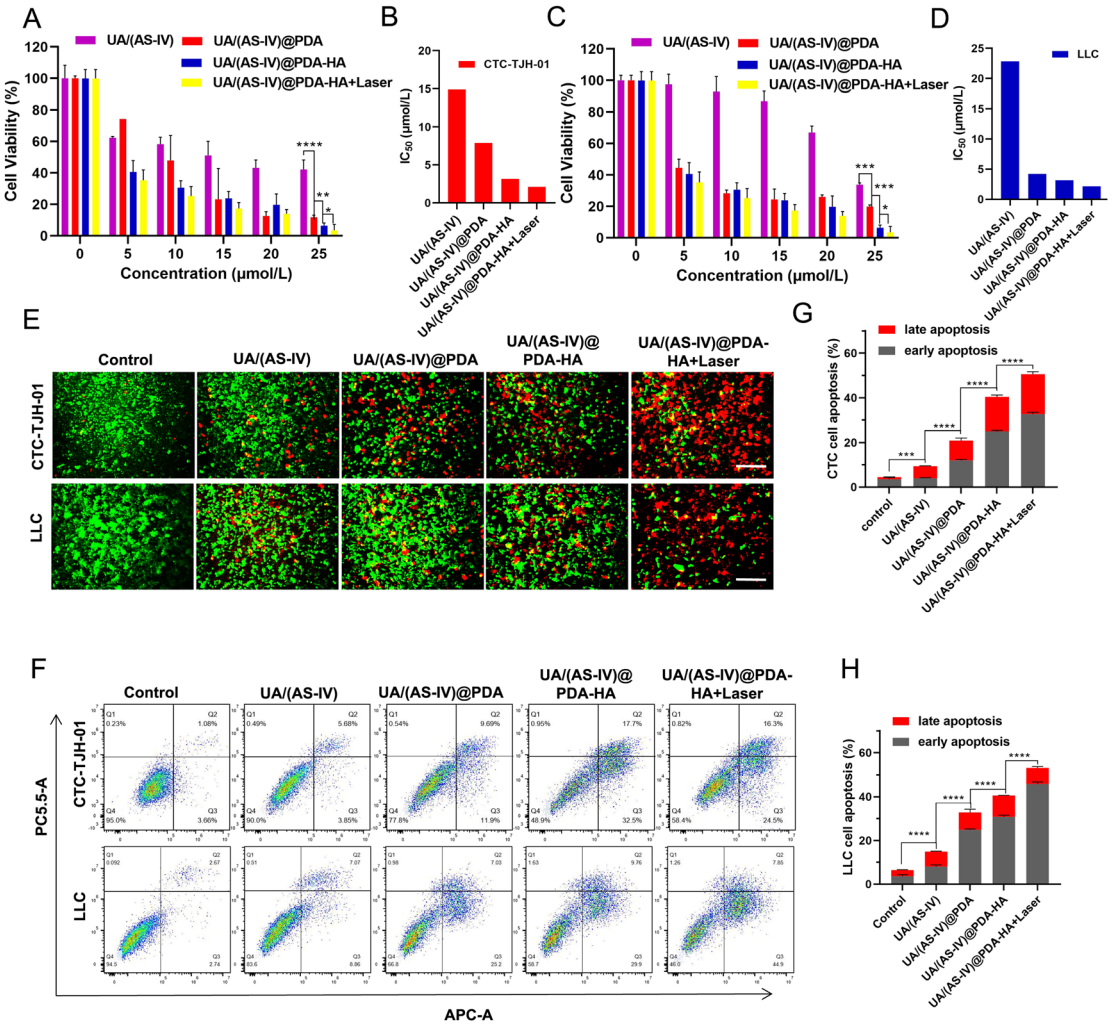

Fig. 5 *In vitro* anti-tumor activity. (A) CCK-8 cell survival rate of CTC-TJH-01 co-incubation with different components after 48 h and (B) the corresponding IC_{50} value (CTC-TJH-01 cell line). (C) CCK-8 cell survival rate of LLC-luc co-incubation with different components after 48 h and (D) the corresponding IC_{50} value (LLC-luc cell line). (E) Analysis of cell survival of different treatment with Calcein-AM/PI alive/dead staining. The green signal from Calcein-AM indicated live cells, and the red signal from PI indicated dead cells. Scale bars = 100 μm. (F)–(H) Flow cytometry analysis to study the apoptosis level of CTC-TJH-01 and LLC-luc co-stained with Annexin V-FITC and PI for different treatments. Data are presented as mean ± SD (n = 3). $^{*}p < 0.05$, $^{**}p < 0.01$, $^{***}p < 0.001$, $^{****}p < 0.0001$.

through the EPR effect. As for the active targeting ability of HA, the CCK-8 assay was performed for UA/(AS-IV)@PDA-HA. Compared to UA/(AS-IV)@PDA, UA/(AS-IV)@PDA-HA markedly suppressed the cell proliferation of CTC-TJH-01 (IC_{50} = 3.17 μM, 48 h) and LLC-luc (IC_{50} = 3.167 μM, 48 h). This may be because UA/(AS-IV)@PDA-HA could realize specific accumulation at the tumor site due to the active targeting specificity of HA for cancer cells overexpressing the CD44 receptor. In addition, UA/(AS-IV)@PDA-HA with 808 nm laser irradiation resulted in the highest therapeutic efficacy *in vitro*, effectively inhibiting the viability of CTC-TJH-01 (IC_{50} = 2.129 μM, 48 h) and LLC-luc (IC_{50} = 2.147 μM, 48 h), indicating that the nanomedicine possesses outstanding PTT ability. Taken together, the results indicate that UA/(AS-IV)@PDA-HA plus PTT displayed the highest anti-tumor efficacy *in vitro* against lung cancer cells compared to free UA/(AS-IV) drugs.

In addition, calcein-AM/PI staining and apoptosis experiments demonstrated the remarkable cell lethality of nanomedicines (Fig. 5(E)), which was consistent with the results of the cytotoxicity assay. The apoptosis rate (including early apoptosis and late apoptosis) induced by the delivery of different medicines was analyzed in CTC-TJH-01 and LLC-luc cells (Fig. 5(F)–(H)). The resulting apoptotic ratios of cells treated with free UA/(AS-IV), UA/(AS-IV)@PDA, UA/(AS-IV)@PDA-HA, and UA/(AS-IV)@PDA-HA with 808 nm laser irradiation in CTC-TJH-01 were 9.44%, 20.91%, 40.36% and 50.56%, respectively. The apoptotic ratios of cells treated with free UA/(AS-IV), UA/(AS-IV)@PDA, UA/(AS-IV)@PDA-HA, and UA/(AS-IV)@PDA-HA with 808 nm laser irradiation in LLC-luc were 14.92%, 32.78%, 40.56%, and 53.06%, respectively. The apoptosis experiment further indicated that nanomedicines better induce apoptotic processes. Additionally, HA, NIR irradiation could efficiently promote the apoptosis of CTC-TJH-01 and LLC-luc cells.

3.7 *In vitro* anti-metastasis effect

Cell migration and invasion play crucial roles in lung cancer metastasis. To investigate the effect of the formulated nanomedicine on cell migration, a scratch wound healing assay was performed (Fig. 6(A)). The process of wound closure in the scratched area by migratory cells was monitored using inverted microscopy after 24 h. Wound healing closure was calculated using ImageJ software (Fig. 6(D)). As indicated by the results, CTC-TJH-01 and LLC-luc without treatment exhibited a marked wound healing ability, with 78% and 94.83% wound closure

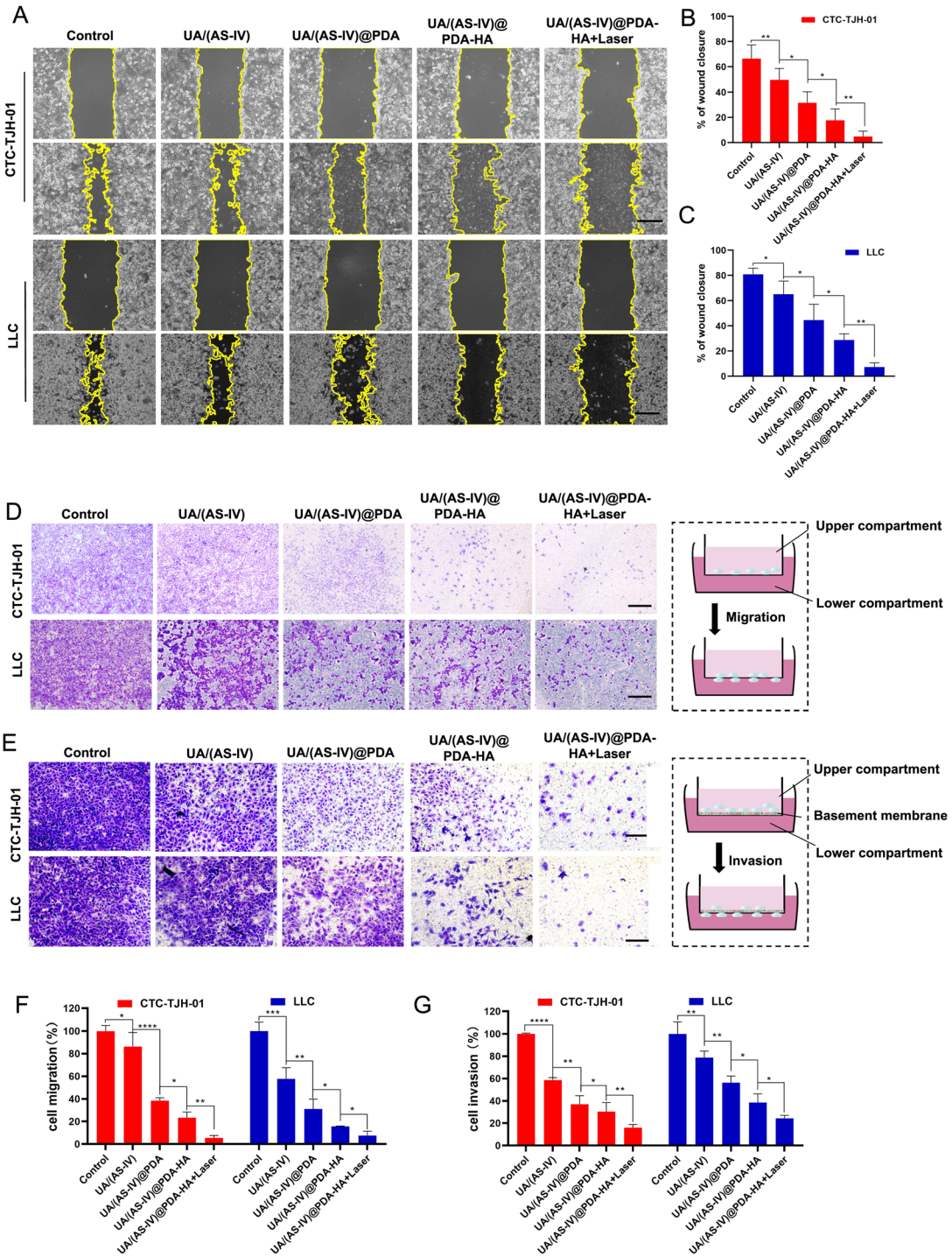

Fig. 6 *In vitro* anti-metastatic efficacy. (A)–(C) Microscopic images of time-dependent wound gaps after different treatments indicating the migratory ability of CTC-TJH-01 and LLC-luc. Scale bars = 50 μm. (D) and (F) Assessment of migration with different treatments *in vitro* after 24 h. Scale bars = 100 μm. (E) and (G) Assessment of invasion with different treatments *in vitro* after 24 h. Scale bars = 50 μm. *$p < 0.05$, **$p < 0.01$, ***$p < 0.001$, ****$p < 0.0001$.

after 24 h of incubation, demonstrating the intense metastatic characteristics of lung cancer cells. Free UA/AS-IV had a minor inhibitory effect on the wound healing ability of lung cancer cells. However, nanomedicines can significantly inhibit cell motility due to their high efficiency of delivery capacity through the EPR effect. HA-mediated targeted delivery may be better for inhibiting cell migration. Notably, cells co-treated with UA/(AS-IV)@PDA-HA under 808 nm laser irradiation showed only 22% wound closure (CTC-TJH-01) and 0% wound closure (LLC-luc) with negligible cell motility.

Next, a Transwell migration assay was used to evaluate the effect of the formulated nanomedicines on cell migration (Fig. 6(B)). Similar results were observed in the wound-healing assay. In the control group, the migrating cells displayed almost the entire lower surface of the Transwell chamber. Free UA/(AS-IV) showed a slight inhibitory effect on cell migration ability, while nanomedicines notably suppressed cell migration, with fewer migrating cells on the lower surface. In particular, the fewest cells were displayed on the lower surface of the Transwell chamber after combined treatment with UA/(AS-IV)@PDA-HA NPs and 808 nm laser irradiation (Fig. 6(E)). These results demonstrate that the combination of UA/(AS-IV) nanomedicine with PTT is beneficial for inhibiting lung cancer cell migration *in vitro*.

To evaluate the effect of the formulated nanoparticles on cell invasion, a Transwell invasion assay was performed. Free UA/(AS-IV) showed a slight inhibitory effect on cell invasion ability (Fig. 6(C)). However, nanomedicines notably suppressed cell invasion, with fewer cells on the lower surface. UA/(AS-IV)@PDA-HA significantly inhibited cancer cell migration. In particular, the fewest cells were displayed on the lower surface of the Transwell chamber by the combined treatment of UA/(AS-IV)@PDA-HA with 808 nm laser irradiation (Fig. 6(F)). These results demonstrate that the combination of UA/(AS-IV) nano-delivery and PTT is beneficial for inhibiting lung cancer cell invasion *in vitro*.

3.8 *In vivo* photothermal experiment

To explore drugs that inhibit the growth of lung cancer cells *in vivo*, LLC-luc tumor-bearing mice were divided into four groups, which each received intraperitoneal injections of either saline, free UA/(AS-IV), UA/(AS-IV)@PDA, or UA/(AS-IV)@PDA-HA. First, the PTT of the nanomedicine *in vivo* was tested. The tumor temperature changes of the mice with various treatments were recorded using an IR thermal camera 24 h post-injection. Then, the tumours in the mice were irradiated with an 808 nm laser for 5 min at a power density of 1.0 W cm^{-2} (Fig. 7(A)). The spatial temperature distribution and temperature

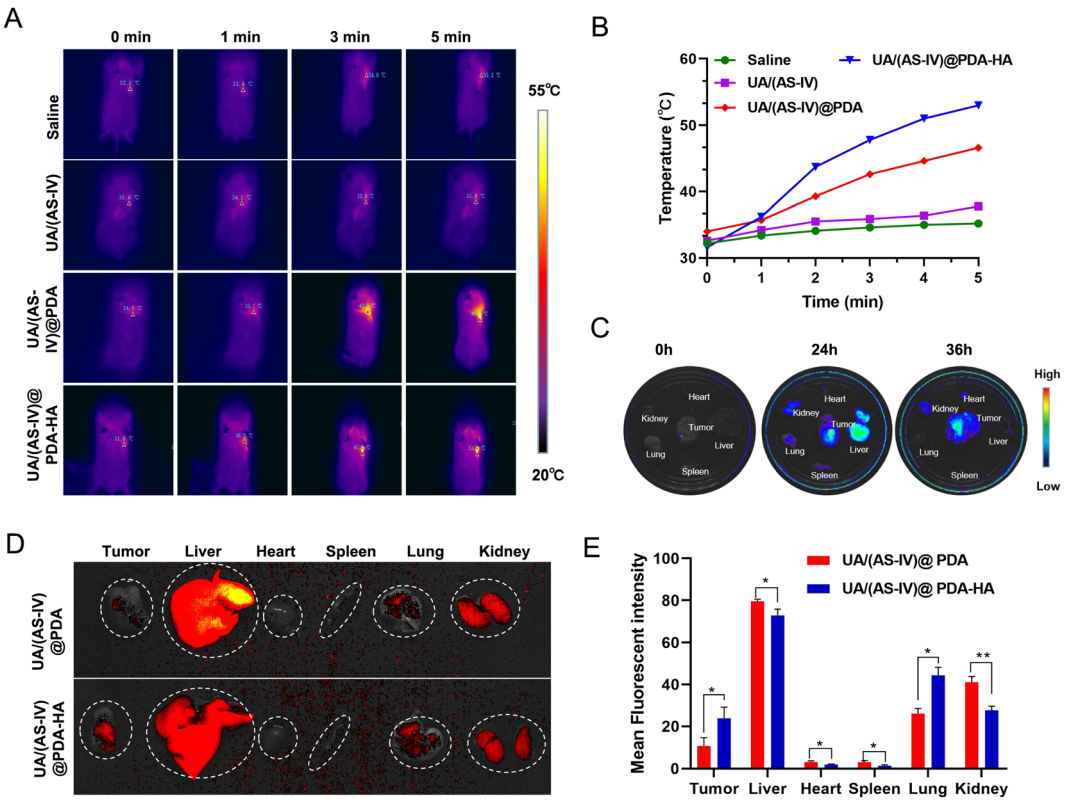

Fig. 7 *In vivo* photothermal experiment and biodistribution. (A) Representative photothermal images LLC-luc tumor-bearing C57BL/6 mice under 808 nm laswer irradiation (1.0 W cm^{-2}, 5 min) after 12 h injected intraperitoneally with saline, UA/(AS-IV), UA(AS-IV)@PDA and UA/(AS-IV)@PDA-HA and (B) The corresponding temperature rise curves of the tumor region of mice over 5 min irradiation. (C) *In vivo* biodistribution of UA/(AS-IV)@PDA-HA. (D) Bioluminescence images of UA(AS-IV)@PDA and UA/(AS-IV)@PDA-HA distribution *in vivo* 24 h after administration and (E) the corresponding fluorescence semi-quantification ($n = 3$). *$p < 0.05$, **$p < 0.01$.

increase at the tumor sites were monitored in real-time using an IR imaging camera. The temperature of the tumor region in the NP-injected group was found to increase rapidly under 1 W cm^{-2} laser irradiation (Fig. 7(B)). However, the temperature of the tumor region of the saline-injected group and free UA/(AS-IV)-injected group did not show any obvious increase, even under 1 W cm^{-2} laser irradiation. This difference in temperature was attributed to the good photothermal conversion efficiency of the PDA nanomaterial. In addition, the temperature of the UA/(AS-IV)@PDA-HA-treated tumor site was higher than that of the non-targeted UA/(AS-IV)@PDA-treated tumor site due to the specific targeting of HA-modified nanoparticles to tumor cells, which causes more drugs to accumulate at the tumor site for enhanced therapeutic efficiency. These results indicate that UA/(AS-IV)@PDA-HA possesses a high photothermal conversion capability for potential applications in PTT.

3.9 *In vivo* biodistribution and HA-mediated acting targeting

To monitor the distribution *in vivo*, fluorescently labelled UA/(AS-IV)@PDA and UA/(AS-IV)@PDA-HA were injected intraperitoneally into LLC-luc tumor-bearing mice. After either 24 or 36 h of injection, the mice were sacrificed, and the main organs and tumors were isolated for *ex vivo* imaging. As a result, the fluorescence intensity in the tumors and main organs was found to increased gradually over time from 0 to 24 h (Fig. 7(C)). Nanomedicine accumulation in the tumors was highest at 24 h. Similarly, the nanomedicine content in the different organs (*e.g.*, heart, liver, spleen, lungs, and kidneys) and tumors was also detected within 24 h. Nanomedicine was found to mainly accumulate in the liver, kidneys and tumors (Subcutaneous tumor and Lung metastasis).

In addition, we found that tumors (Subcutaneous tumor and Lung metastasis) in the UA/(AS-IV)@PDA-HA group exhibited stronger fluorescence intensity than those in the UA/(AS-IV)@PDA group, whereas main organs (heart, liver, spleen and kidneys) in the UA/(AS-IV)@PDA-HA group exhibited Lower fluorescence intensity than those in the UA/(AS-IV)@PDA group (Fig. 7(D) and (E)). The result demonstrates that the HA-modified nanomedicine aggregated better at tumor sites and aggregated less at normal tissue due to the HA-mediated active targeting ability.

3.10 (AS-IV)-mediated immune response

In addition, nanomedicine further remodels the immunosuppressive microenvironment to suppress lung cancer metastasis. Immunohistochemical (IHC) experiments in subcutaneous tumors and lung metastasis foci were performed to investigate the immune status change. Since $CD8^+$ T and NK cells are crucial for the regulating immune response, we evaluated the levels of these T cells in subcutaneous tumors (primary tumors) and in lung metastatic foci. The number of $CD8^+$ T cells and NK cells in the primary tumors was found to be significantly increased in UA/(AS-IV)@PDA-HA compared to groups treated with free UA/(AS-IV) (Fig. 8(A)–(C)). Furthermore, the number of $CD8^+$ T cells and NK cells in the lung metastatic foci was also significantly increased in UA/(AS-IV)@PDA-HA compared to the groups treated with free UA/(AS-IV) (Fig. 8(D)–(F)). These comparisons indicate that the nanomedicine induced stronger anti-tumor immunity in the LLC-luc tumor model.

3.11 *In vivo* anti-tumor effect

The mice were stochastically divided into five groups (n = 6): (i) saline (0.9% NaCl solution), (ii) free UA/(AS-IV),

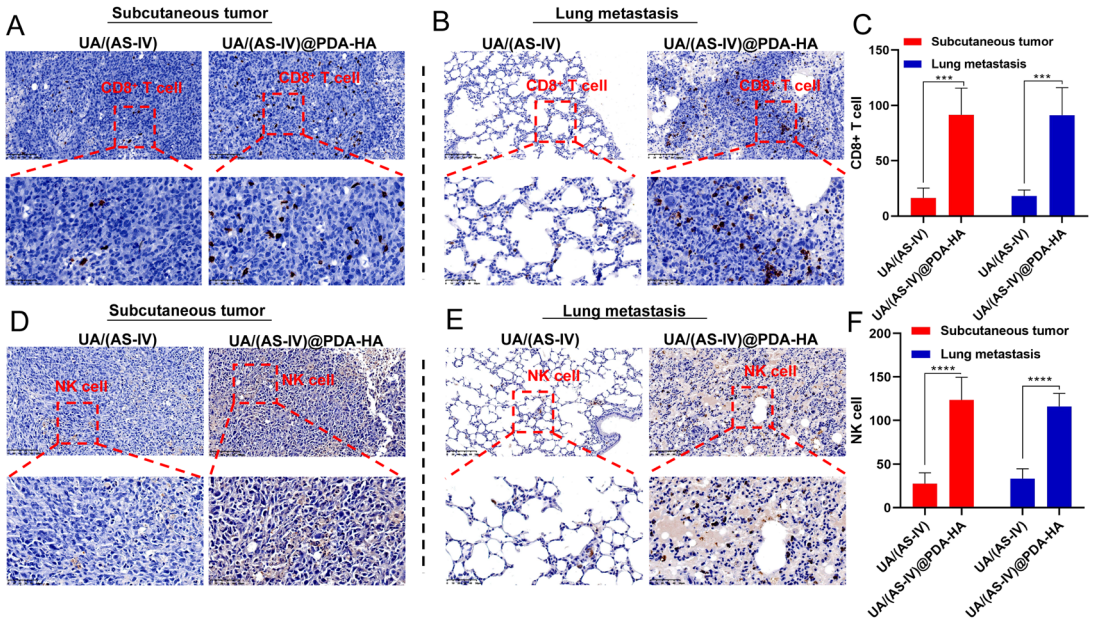

Fig. 8 Immunofluorescence staining results of CD8-positive T cells in (A) subcutaneous tumor and (B) lung metastasis. (C) The corresponding quantification of the number of CD8-positive T cells in subcutaneous tumor and lung metastasis. Immunofluorescence staining results of NK cells in (D) subcutaneous tumor and (E) lung metastasis. (F) The corresponding quantification of the number of NK cells in subcutaneous tumor and lung metastasis. ***$p < 0.001$, ****$p < 0.0001$. Scale bar = 100 μm, 50 μm.

(iii) UA/(AS-IV)@PDA, (iv) UA/(AS-IV)@PDA-HA, and (v) UA/(AS-IV)@PDA-HA with 808 nm laser irradiation (1 W cm^{-2}, 5 min) (Fig. 9(A)). The resulting anti-tumor efficiency was evaluated in LLC-luc-bearing mice. Among the groups, the tumor volumes of mice injected with free UA/(AS-IV) alone showed only marginally suppressed tumor proliferation (Fig. 9(B) and (C)). However, treatment with nanomedicine resulted in a marked decrease in the tumor volume. In addition, UA/(AS-IV)@PDA-HA-treated mice exhibited a stronger delay in tumor growth and a greater therapeutic efficiency than UA/(AS-IV)@PDA mice due to HA-mediated cellular targeting. Strikingly, UA/(AS-IV)@PDA-HA-treated mice with 808 nm laser irradiation exhibited the strongest tumor growth inhibition compared with all other groups because of PTT. The different therapeutic efficacies were also confirmed by the weight of the tumor after the mice were sacrificed at the final stage of the *in vivo* studies. This is consistent with the changes in tumor growth and tumor weight results. These results were further confirmed by H&E, caspase-3 (Fig. 9(D)), and Ki-67 staining of tumors after treatment. Taken together, the results indicate that NPs can effectively inhibit tumorigenesis, demonstrating excellent therapeutic efficacy *in vivo*, wherein the combination of chemo-immuno-PTT markedly inhibited tumor growth.

3.12 *In vivo* anti-metastasis effect

To evaluate the anti-metastatic efficacy of each treatment, we established a mouse lung metastasis model. At the end of the administration period, over 15 metastatic nodules were found in the lungs of mice injected with saline and free UA/(AS-IV), indicating severe lung metastasis (Fig. 10(A) and (C)). Fortunately, the nanomedicines administered were found to effectively inhibit lung cancer metastasis in the corresponding treatment groups. A histopathological examination of the lung sections further confirmed tumor metastasis (Fig. 10(B) and (D)). Compared to the control group, the administration of free UA/(AS-IV) alone showed a slight anti-metastatic effect on the tumors. However, UA/(AS-IV)@PDA, UA/(AS-IV)@PDA-HA, and UA/(AS-IV)@PDA-HA combined with 808 nm irradiation was found to significantly suppress tumor metastasis, with negligible metastatic nodules and a small area of tumor burden observed in the tissue slides. Owing to the excellent anti-tumor effects, almost no tumor burden area appeared in the H&E staining images of mice treated with UA/(AS-IV)@PDA-HA with 808 nm irradiation, which suggested an attenuated risk of tumor metastasis. Taken together, these results indicate that the combination of chemo-immuno-PTT appears to be a promising therapeutic strategy for metastatic lung cancer, based

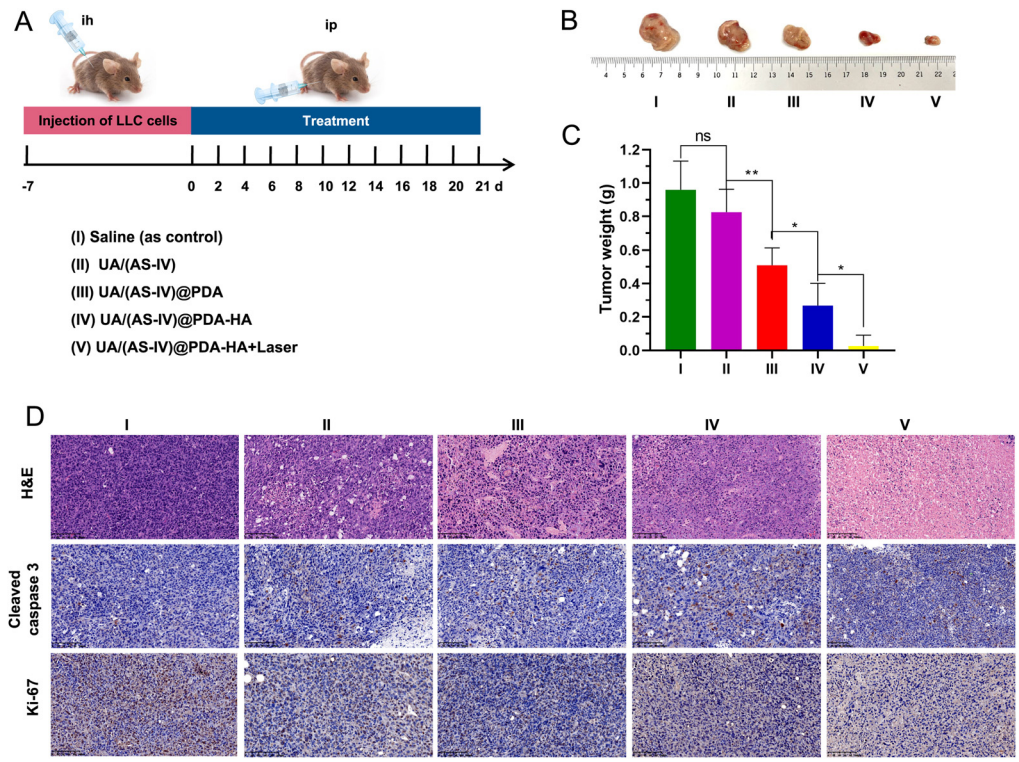

Fig. 9 *In vivo* anti-tumor effect. (A) Schematic illustration for the establishment of a subcutaneous tumorigenic and lung metastasis model and subsequent treatment regime. (B) Representative photographs of excised subcutaneous tumors after different treatments on day 21. (C) Relative subcutaneous tumor weight after 21 d with different treatments during the therapy period. (D) H&E-stained subcutaneous tumor slices (scale bar =100 μm) collected from mice and immunohistochemistry staining results of Cleaved caspase 3 and Ki-67 of subcutaneous tumor tissue slices (scale bar =50 μm) obtained from mice on day 21. (I) Saline, (II) UA/(AS-IV), (III) UA/(AS-IV)@PDA, (IV) UA/(AS-IV)@PDA-HA, (V) UA/(AS-IV)@PDA-HA under 808 nm laser irradiation (1.0 W cm^{-2}, 5 min), and $*p < 0.05$, $**p < 0.01$.

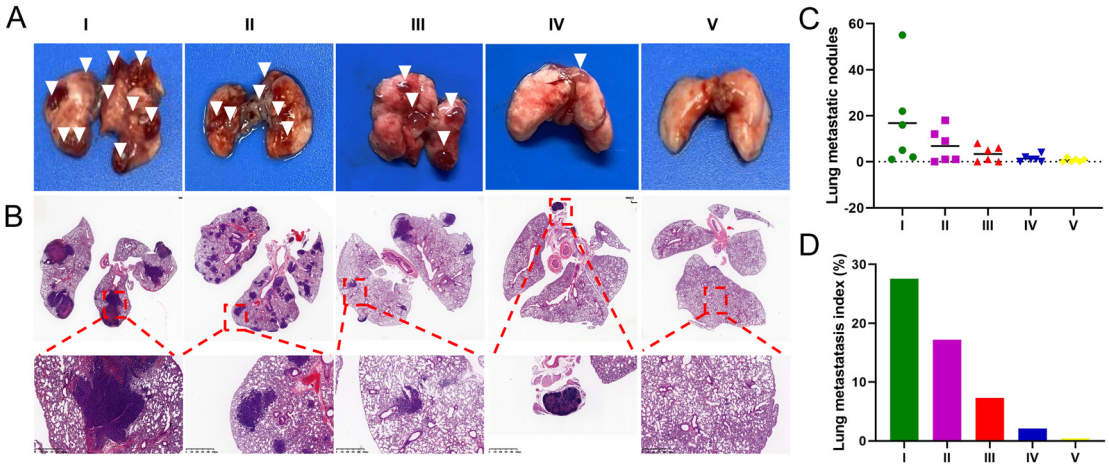

Fig. 10 *In vivo* anti-metastatic efficacy. (A) Representative photos of the metastasis in the lung after different treatments on day 21. (B) H&E-stained lung sections (scale bar = 100 μm, 50 μm) collected from mice on day 21. (C) Lung metastasis nodules after different treatment. (D) Lung metastasis index after different treatment, calculated by (lung tumor area/lung area) × 100. (I) Saline, (II) UA/(AS-IV), (III) UA/(AS-IV)@PDA, (IV) UA/(AS-IV)@PDA-HA, (V) UA/(AS-IV)@PDA-HA under 808 nm laser irradiation (1.0 W cm^{-2}, 5 min).

on the effective inhibition of the proliferation of orthotopic tumors and the excellent restriction of lung cancer metastasis.

3.13 *In vivo* biocompatibility evaluation

LLC-luc tumor-bearing mice were injected intraperitoneally for three weeks to assess the potential toxicity of UA/(AS-IV)@PDA-HA. None of the mice died during the treatment period. The body weight of the mice showed no apparent changes during treatment among the different groups (Fig. 11(B)). The major organs were harvested from the mice at the end of the treatment. To further explore biocompatibility *in vivo*, H&E staining of the major organs was performed after treatment. H&E staining analysis of the heart, liver, spleen, lung, and kidneys in all treatment groups showed no obvious damage in comparison with the control group (Fig. 11(A)). These results further indicated the good compatibility of the nanomedicine.

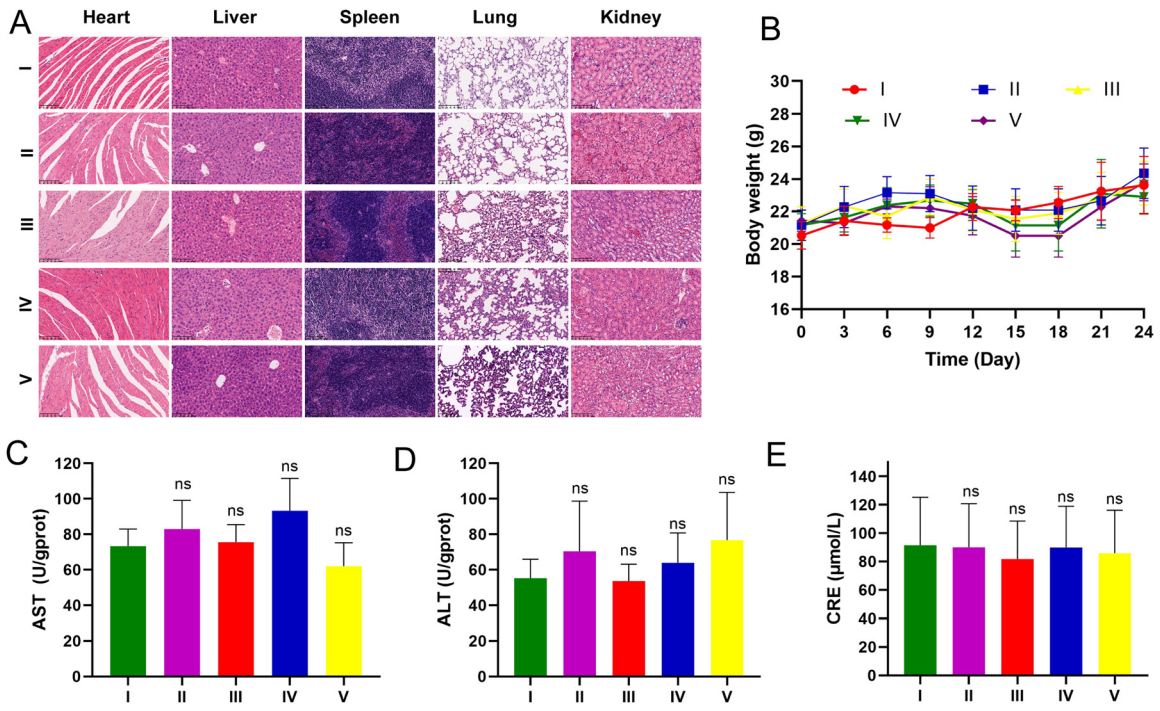

Fig. 11 Long-term *in vivo* toxicity. (A) H&E staining images of major organs (heart, liver, spleen, lung, and kidney) of mice after different treatment, scale bar = 100 μm. (B) Weight of mice after different treatments. (C) Alanine aminotransferase (ALT). (D) Aspartate aminotransferase (AST) and (E) Creatinine (CRE). (I) Saline, (II) UA/(AS-IV), (III) UA/(AS-IV)@PDA, (IV) UA/(AS-IV)@PDA-HA, (V) UA/(AS-IV)@PDA-HA under 808 nm laser irradiation (1.0 W cm^{-2}, 5 min).

Furthermore, we evaluated hepatorenal toxicity in mice, and no apparent toxicity was observed among the different treatments (Fig. 11(C)–(E)). These results confirmed the safety of free UA/(AS-IV), UA/(AS-IV)@PDA, UA/(AS-IV)@PDA-HA, and UA/(AS-IV)@PDA-HA with 808 nm laser irradiation. Collectively, these results suggest that the nanoformulation is safe and tolerable *in vivo* at the selected dose.

4. Conclusion

In this study, we developed a UA/(AS-IV)-loaded HA-modified PDA nanomedicine, referred to as UA/(AS-IV)@PDA-HA. This is a synergistic therapy of chemo-immuno-PTT, with active tumor-targeting ability, for highly effective anti-primary tumor and anti-distant metastasis treatment. The results presented herein demonstrated that UA/(AS-IV)@PDA-HA: (i) exhibits excellent photothermal conversion efficiency in the NIR-I window based on PDA nanomaterial, using light to destroy cancer cells by heat; (ii) actively targeted NSCLC based on HA-modified nanomedicine; (iii) has good biocompatibility; (iv) shows UA-mediated cytotoxicity, effectively inhibiting proliferation and metastasis; (v) shows great promise in (UA-IV)-mediated anticancer immunotherapy to inhibit the growth and metastasis of NSCLC. Overall, UA/(AS-IV)@PDA-HA was found to be a promising medication for the effective treatment of primary and metastatic NSCLC. The effectiveness of the nano-drug was superior to that of free UA/(AS-IV). Thus, this study provides important insights for the clinical management of lung cancer growth and metastasis.

Ethical standards

For the animal study, the study protocol was approved by the Animal Ethics Committee of Shanghai University of Traditional Chinese Medicine.

Author contributions

The work was completed through contributions of all authors. All authors have given approval to the final version of this article.

Conflicts of interest

The authors declare that they have no conflict of interest.

Acknowledgements

This work was financially supported by Shanghai Frontier Research Base of Disease and Syndrome Biology of Inflammatory cancer transformation (2021KJ03-12), Future plan for Traditional Chinese Medicine Inheritance and Development of Shanghai Municipal Hospital of Traditional Chinese Medicine (WLJH2021ZY-MZY020), Natural Science Foundation of Shanghai (20ZR1459100) and Biomedical Science and Technology Support Project of Shanghai (22S11900800).

References

1 H. Sung, J. Ferlay, R. L. Siegel, M. Laversanne, I. Soerjomataram, A. Jemal and F. Bray, Global Cancer Statistics 2020: GLOBOCAN Estimates of Incidence and Mortality Worldwide for 36 Cancers in 185 Countries, *Ca-Cancer J. Clin.*, 2021, **71**, 209–249.
2 R. L. Siegel, K. D. Miller, H. E. Fuchs and A. Jemal, Cancer statistics, 2022, *Ca-Cancer J. Clin.*, 2022, **72**, 7–33.
3 A. Friedlaender, A. Addeo, A. Russo, V. Gregorc, D. Cortinovis and C. D. Rolfo, Targeted Therapies in Early Stage NSCLC: Hype or Hope?, *Int. J. Mol. Sci.*, 2020, **21**, 6329–6340.
4 L. Galluzzi, J. Humeau, A. Buqué, L. Zitvogel and G. Kroemer, Immunostimulation with chemotherapy in the era of immune checkpoint inhibitors, *Nat. Rev. Clin. Oncol.*, 2020, **17**, 725–741.
5 E. Quoix, R. Ramlau, V. Westeel, Z. Papai, A. Madroszyk, A. Riviere, P. Koralewski, J. L. Breton, E. Stoelben and D. Braun, *et al.*, Therapeutic vaccination with TG4010 and first-line chemotherapy in advanced non-small-cell lung cancer: a controlled phase 2B trial, *Lancet Oncol.*, 2011, **12**, 1125–1133.
6 S. K. Jabbour, S. M. Keller and M. Reck, Analysis of Outcomes With Addition of Immunotherapy to Chemoradiation Therapy for Non-Small Cell Lung Cancer-Reply, *JAMA Oncol.*, 2022, **8**, 168–169.
7 M. Reck, J. Remon and M. D. Hellmann, First-Line Immunotherapy for Non-Small-Cell Lung Cancer, *J. Clin. Oncol.*, 2022, **40**, 586–597.
8 F. Sonvico, S. Mornet, S. Vasseur, C. Dubernet, D. Jaillard, J. Degrouard, J. Hoebeke, E. Duguet, P. Colombo and P. Couvreur, Folate-conjugated iron oxide nanoparticles for solid tumor targeting as potential specific magnetic hyperthermia mediators: synthesis, physicochemical characterization, and *in vitro* experiments, *Bioconjugate Chem.*, 2005, **16**, 1181–1188.
9 A. Coates, S. Abraham, S. B. Kaye, T. Sowerbutts, C. Frewin, R. M. Fox and M. H. Tattersall, On the receiving end--patient perception of the side-effects of cancer chemotherapy, *Eur. J. Cancer Clin. Oncol.*, 1983, **19**, 203–208.
10 E. B. Garon, N. A. Rizvi, R. Hui, N. Leighl, A. S. Balmanoukian, J. P. Eder, A. Patnaik, C. Aggarwal, M. Gubens and L. Horn, *et al.*, Pembrolizumab for the treatment of non-small-cell lung cancer, *N. Engl. J. Med.*, 2015, **372**, 2018–2028.
11 J. Brahmer, K. L. Reckamp, P. Baas, L. Crinò, W. E. Eberhardt, E. Poddubskaya, S. Antonia, A. Pluzanski, E. E. Vokes and E. Holgado, *et al.*, Nivolumab versus Docetaxel in Advanced Squamous-Cell Non-Small-Cell Lung Cancer, *N. Engl. J. Med.*, 2015, **373**, 123–135.
12 U. Nitz, O. Gluz, M. Graeser, M. Christgen, S. Kuemmel, E. M. Grischke, M. Braun, D. Augustin, J. Potenberg and

K. Krauss, *et al.*, De-escalated neoadjuvant pertuzumab plus trastuzumab therapy with or without weekly paclitaxel in HER2-positive, hormone receptor-negative, early breast cancer (WSG-ADAPT-HER2+/HR-): survival outcomes from a multicentre, open-label, randomised, phase 2 trial, *Lancet Oncol.*, 2022, **23**, 625–635.

13 C. Falandry, F. Rousseau, M. A. Mouret-Reynier, F. Tinquaut, D. Lorusso, J. Herrstedt, A. M. Savoye, L. Stefani, E. Bourbouloux and R. Sverdlin, *et al.*, Efficacy and Safety of First-line Single-Agent Carboplatin *vs.* Carboplatin Plus Paclitaxel for Vulnerable Older Adult Women With Ovarian Cancer: A GINECO/GCIG Randomized Clinical Trial, *JAMA Oncol.*, 2021, **7**, 853–861.

14 M. Sun, Y. Ye, L. Xiao, X. Duan, Y. Zhang and H. Zhang, Anticancer effects of ginsenoside Rg3 (Review), *Int. J. Mol. Med.*, 2017, **39**, 507–518.

15 W. Weng and A. Goel, Curcumin and colorectal cancer: An update and current perspective on this natural medicine, *Semin. Cancer Biol.*, 2022, **80**, 73–86.

16 J. U. Marquardt, L. Gomez-Quiroz, C. L. Arreguin, F. Pinna, Y. H. Lee, M. Kitade, M. P. Domínguez, D. Castven, K. Breuhahn and E. A. Conner, *et al.*, Curcumin effectively inhibits oncogenic NF-κB signaling and restrains stemness features in liver cancer, *J. Hepatol.*, 2015, **63**, 661–669.

17 H. H. Cao, C. Y. Cheng, T. Su, X. Q. Fu, H. Guo, T. Li, A. K. Tse, H. Y. Kwan, H. Yu and Z. L. Yu, Quercetin inhibits HGF/c-Met signaling and HGF-stimulated melanoma cell migration and invasion, *Mol. Cancer*, 2015, **14**, 103–115.

18 C. C. Nwaeburu, A. Abukiwan, Z. Zhao and I. Herr, Quercetin-induced miR-200b-3p regulates the mode of self-renewing divisions in pancreatic cancer, *Mol. Cancer*, 2017, **16**, 23–33.

19 C. Li, J. Chen, W. Yuan, W. Zhang, H. Chen and H. Tan, Preventive effect of ursolic acid derivative on particulate matter 2.5-induced chronic obstructive pulmonary disease involves suppression of lung inflammation, *IUBMB Life*, 2020, **72**, 632–640.

20 S. Tang, C. Fang, Y. Liu, L. Tang and Y. Xu, Anti-obesity and Anti-diabetic Effect of Ursolic Acid against Streptozotocin/High Fat Induced Obese in Diabetic Rats, *J. Oleo Sci.*, 2022, **71**, 289–300.

21 K. Yang, Y. Chen, J. Zhou, L. Ma, Y. Shan, X. Cheng, Y. Wang, Z. Zhang, X. Ji and L. Chen, *et al.*, Ursolic acid promotes apoptosis and mediates transcriptional suppression of CT45A2 gene expression in non-small-cell lung carcinoma harbouring EGFR T790M mutations, *Br. J. Pharmacol.*, 2019, **176**, 4609–4624.

22 M. Wang, H. Yu, R. Wu, Z. Y. Chen, Q. Hu, Y. F. Zhang, S. H. Gao and G. B. Zhou, Autophagy inhibition enhances the inhibitory effects of ursolic acid on lung cancer cells, *Int. J. Mol. Med.*, 2020, **46**, 1816–1826.

23 K. Liu, L. Guo, L. Miao, W. Bao, J. Yang, X. Li, T. Xi and W. Zhao, Ursolic acid inhibits epithelial-mesenchymal transition by suppressing the expression of astrocyte-elevated gene-1 in human nonsmall cell lung cancer A549 cells, *Anticancer Drugs*, 2013, **24**, 494–503.

24 A. Zhang, Y. Zheng, Z. Que, L. Zhang, S. Lin, V. Le, J. Liu and J. Tian, Astragaloside IV inhibits progression of lung cancer by mediating immune function of Tregs and CTLs by interfering with IDO, *J. Cancer Res. Clin. Oncol.*, 2014, **140**, 1883–1890.

25 F. Xu, W. Q. Cui, Y. Wei, J. Cui, J. Qiu, L. L. Hu, W. Y. Gong, J. C. Dong and B. J. Liu, Astragaloside IV inhibits lung cancer progression and metastasis by modulating macrophage polarization through AMPK signaling, *J. Exp. Clin. Cancer Res.*, 2018, **37**, 207–223.

26 P. Zhang, Y. Zhai, Y. Cai, Y. Zhao and Y. Li, Nanomedicine-Based Immunotherapy for the Treatment of Cancer Metastasis, *Adv. Mater.*, 2019, **31**, 49–67.

27 J. Zhang, L. Shen, X. Li, W. Song, Y. Liu and L. Huang, Nanoformulated Codelivery of Quercetin and Alantolactone Promotes an Antitumor Response through Synergistic Immunogenic Cell Death for Microsatellite-Stable Colorectal Cancer, *ACS Nano*, 2019, **13**, 12511–12524.

28 T. Ma, Y. Liu, Q. Wu, L. Luo, Y. Cui, X. Wang, X. Chen, L. Tan and X. Meng, Quercetin-Modified Metal–Organic Frameworks for Dual Sensitization of Radiotherapy in Tumor Tissues by Inhibiting the Carbonic Anhydrase IX, *ACS Nano*, 2019, **13**, 4209–4219.

29 X. Guan, Cancer metastases: challenges and opportunities, *Acta Pharm. Sin. B*, 2015, **5**, 402–418.

30 M. Xiao, J. Fan, M. Li, F. Xu, X. Zhao, D. Xi, H. Ma, Y. Li, J. Du and W. Sun, *et al.*, A photosensitizer-inhibitor conjugate for photodynamic therapy with simultaneous inhibition of treatment escape pathways, *Biomaterials*, 2020, **257**, 120262.

31 F. Chen, Y. Xing, Z. Wang, X. Zheng, J. Zhang and K. Cai, Nanoscale Polydopamine (PDA) Meets π–π Interactions: An Interface-Directed Coassembly Approach for Mesoporous Nanoparticles, *Langmuir*, 2016, **32**, 12119–12128.

32 Y. Chen, K. Ai, J. Liu, X. Ren, C. Jiang and L. Lu, Polydopamine-based coordination nanocomplex for T1/T2 dual mode magnetic resonance imaging-guided chemo-photothermal synergistic therapy, *Biomaterials*, 2016, **77**, 198–206.

33 B. Li, T. Gong, N. Xu, F. Cui, B. Yuan, Q. Yuan, H. Sun, L. Wang and J. Liu, Improved Stability and Photothermal Performance of Polydopamine-Modified $Fe_{(3)}O_{(4)}$ Nanocomposites for Highly Efficient Magnetic Resonance Imaging-Guided Photothermal Therapy, *Small*, 2020, **16**, 45–64.

34 A. J. McGrath, Y. H. Chien, S. Cheong, D. A. Herman, J. Watt, A. M. Henning, L. Gloag, C. S. Yeh and R. D. Tilley, Gold over Branched Palladium Nanostructures for Photothermal Cancer Therapy, *ACS Nano*, 2015, **9**, 12283–12291.

35 F. Zhou, S. Wu, S. Song, W. R. Chen, D. E. Resasco and D. Xing, Antitumor immunologically modified carbon nanotubes for photothermal therapy, *Biomaterials*, 2012, **33**, 3235–3242.

36 G. Song, C. Liang, H. Gong, M. Li, X. Zheng, L. Cheng, K. Yang, X. Jiang and Z. Liu, Core–Shell MnSe@Bi_2Se_3 Fabricated *via* a Cation Exchange Method as Novel

Nanotheranostics for Multimodal Imaging and Synergistic Thermoradiotherapy, *Adv. Mater.*, 2015, **27**, 6110–6117.

37 B. Shi, N. Ren, L. Gu, G. Xu, R. Wang, T. Zhu, Y. Zhu, C. Fan, C. Zhao and H. Tian, Theranostic Nanoplatform with Hydrogen Sulfide Activatable NIR Responsiveness for Imaging-Guided On-Demand Drug Release, *Angew. Chem., Int. Ed.*, 2019, **58**, 16826–16830.

38 X. R. Song, X. Wang, S. X. Yu, J. Cao, S. H. Li, J. Li, G. Liu, H. H. Yang and X. Chen, Co_9Se_8 nanoplates as a new theranostic platform for photoacoustic/magnetic resonance dual-modal-imaging-guided chemo-photothermal combination therapy, *Adv. Mater.*, 2015, **27**, 3285–3291.

39 G. Tian, X. Zhang, X. Zheng, W. Yin, L. Ruan, X. Liu, L. Zhou, L. Yan, S. Li and Z. Gu, *et al.*, Multifunctional Rbx WO_3 nanorods for simultaneous combined chemo-photothermal therapy and photoacoustic/CT imaging, *Small*, 2014, **10**, 4160–4170.

40 D. Loreth, M. Schuette, J. Zinke, M. Mohme, A. Piffko, S. Schneegans, J. Stadler, M. Janning, S. Loges and S. A. Joosse, *et al.*, CD74 and CD44 Expression on CTCs in Cancer Patients with Brain Metastasis, *Int. J. Mol. Sci.*, 2021, 22.

41 W. Sterlacci, S. Savic, M. Fiegl, E. Obermann and A. Tzankov, Putative stem cell markers in non-small-cell lung cancer: a clinicopathologic characterization, *J. Thorac. Oncol.*, 2014, **9**, 41–49.

42 W. Sun, Y. Du, X. Liang, C. Yu, J. Fang, W. Lu, X. Guo, J. Tian, Y. Jin and J. Zheng, Synergistic triple-combination therapy with hyaluronic acid-shelled PPy/CPT nanoparticles results in tumor regression and prevents tumor recurrence and metastasis in 4T1 breast cancer, *Biomaterials*, 2019, **217**, 119264.

43 Y. Hou, J. Jin, H. Duan, C. Liu, L. Chen, W. Huang, Z. Gao and M. Jin, Targeted therapeutic effects of oral inulin-modified double-layered nanoparticles containing chemotherapeutics on orthotopic colon cancer, *Biomaterials*, 2022, **283**, 121440.

44 D. Wang, J. Huang, X. Wang, Y. Yu, H. Zhang, Y. Chen, J. Liu, Z. Sun, H. Zou and D. Sun, *et al.*, The eradication of breast cancer cells and stem cells by 8-hydroxyquinoline-loaded hyaluronan modified mesoporous silica nanoparticle-supported lipid bilayers containing docetaxel, *Biomaterials*, 2013, **34**, 7662–7673.

